Western Graduate&PostdoctoralStudies

Western University
Scholarship@Western

Electronic Thesis and Dissertation Repository

8-19-2020 2:00 PM

A 3D Printed Axon-Mimetic Diffusion MRI Phantom

Tristan K. Kuehn, *The University of Western Ontario*

Supervisor: Khan, Ali R, *The University of Western Ontario*
Co-Supervisor: Baron, Corey A, *The University of Western Ontario*
A thesis submitted in partial fulfillment of the requirements for the Master of Engineering Science degree in Biomedical Engineering
© Tristan K. Kuehn 2020

Follow this and additional works at: https://ir.lib.uwo.ca/etd

 Part of the Bioimaging and Biomedical Optics Commons

Recommended Citation

Kuehn, Tristan K., "A 3D Printed Axon-Mimetic Diffusion MRI Phantom" (2020). *Electronic Thesis and Dissertation Repository*. 7238.
https://ir.lib.uwo.ca/etd/7238

This Dissertation/Thesis is brought to you for free and open access by Scholarship@Western. It has been accepted for inclusion in Electronic Thesis and Dissertation Repository by an authorized administrator of Scholarship@Western. For more information, please contact wlswadmin@uwo.ca.

Abstract

Diffusion MRI is used to non-invasively characterize the microstructure of the brain. However, the accuracy of the characterization is difficult to verify because no other non-invasive imaging modality provides the same information. This thesis presents a novel 3D printed axon-mimetic (3AM) diffusion MRI phantom, a synthetic object designed to mimic the brain's microstructure.

The phantoms were characterized using microscopy, synchrotron micro-computed tomography, and diffusion MRI, and found to have sufficiently axon-mimetic properties to be useful as diffusion MRI phantoms. A set of phantoms designed to have anatomically realistic and complex fibre structures was used to test the response of diffusion MRI models of white matter to fibre orientation dispersion. All tested models were found to respond to orientation dispersion, but some robust metrics were identified. The studies in this thesis demonstrate that 3AM phantoms are a novel, flexible, and inexpensive tool for validating diffusion MRI models of white matter.

Keywords: Diffusion MRI, Diffusion MRI Modeling, Phantoms, Validation, MRI, Neuroscience

Summary for Lay Audience

Magnetic resonance imaging, or MRI, is often used to generate images that we can use to safely investigate the brain. To answer some questions about the brain and how its different regions are interconnected, we need more detail than standard MRI can provide. In these cases, we can use diffusion MRI, which is sensitive to the way water molecules randomly move around. Axons, the connections between brain cells, are shaped like tubes, so it is easier for water molecules to move along the axons than across them.

We can use models, which mathematically describe what we understand about how axons change the motion of water molecules, to make predictions about the brain from diffusion MRI images. However, there is no other safe way to make the same kinds of predictions about a brain, so it is difficult to know how accurate the predictions from diffusion MRI are. What we can do to assess diffusion MRI model predictions is create artificial objects made of tube-shaped structures that mimic axons. If we make the objects and control the same properties that we investigate in the brain, we can use diffusion MRI models to ask questions about the phantoms, the answers to which we already know. If the diffusion MRI models make accurate predictions about a phantom, they probably also make accurate predictions about real brains.

This thesis presents a new kind of diffusion MRI phantom that is produced by 3D printing with a special material. Part of the 3D printed material forms fibres that dissolve in water, leaving behind holes that are tube-shaped like axons. In the thesis, we show that the tube-shaped holes are small enough to convincingly mimic axons. We then use the phantoms to show that diffusion MRI models do not always make consistent predictions when axons bend and cross.

The phantoms presented in this thesis are inexpensive and make it easier for researchers to make sure diffusion MRI models make accurate predictions even in complex parts of the brain. This will help make diffusion MRI as useful as possible for investigating the brain.

Co-Authorship Statement

The work in Chapter 2 is adapted from the paper "Microstructural characterization and validation of a 3D printed phantom for diffusion MRI", authored by F. M. Mushtaha, T. K. Kuehn, O. El-Deeb, S. A. Rohani, L. W. Helpard, J. Moore, H. Ladak, A. Moehring, C. Baron, and A. R. Khan, which was submitted for publication in Magnetic Resonance in Medicine in July 2020. Farah Mushtaha and I were co-first authors of the paper, under the co-supervision of Corey Baron and Ali Khan. Farah worked with Omar El-Deeb under the supervision of Amanda Moehring to perform the microscopy of the phantom material and Farah performed the analyzed the microscopy images with some help from me. I prepared samples that Alireza Rohani and Luke Helpard, under the supervision of Hanif Ladak, took to the Canadian Light Source and scanned with synchrotron micro-CT. I performed the analysis of the micro-CT image. Farah and I worked together to design and produce the phantoms for dMRI scanning, and I performed the computational analysis of the dMRI scan data with help from Farah.

The work in Chapter 3 is a collaboration between Farah Mushtaha and me, under the co-supervision of Ali Khan and Corey Baron. I wrote the software extension necessary to 3D print the phantoms, worked with Farah to prepare the phantoms, and performed the analysis of the dMRI scan data with help from Farah.

Acknowledgements

I would like to start by thanking my supervisor, Dr. Ali Khan, and co-supervisor, Dr. Corey Baron. Dr. Khan and Dr. Baron both foster deeply supportive and intellectually stimulating lab environments. I am very grateful for their encouragement, enthusiasm, and willingness to share their expertise, and I feel very lucky to have had the opportunity to be mentored by both of them.

I would also like to thank the other members of my advisory committee, Dr. Maria Drangova and Dr. Sandrine de Ribaupierre. Their feedback was always incisive and timely, and I am sure they saved me a lot of heartache over the course of this project.

I would like to thank all the members of the Khan and Baron labs, who were always eager to talk science when I needed to go over a concept or find some inspiration, or just to chat when I needed a break. My experience writing my thesis was so much richer for having known them.

I would like to thank all my family members, who have always supported me and continued to encourage me as I worked toward completing my thesis.

Finally, I would like to thank my partner Nicole, whose love and support means the world to me.

Contents

Abstract ii

Summary for Lay Audience iii

Co-Authorship Statement iv

Acknowledgements v

List of Figures ix

List of Tables xiii

List of Abbreviations and Symbols xiv

1 Introduction 1

1.1 Diffusion MRI 1

1.2 Diffusion MRI models of white matter 5

1.2.1 Diffusion tensor imaging 6

1.2.2 Diffusion kurtosis imaging 7

1.2.3 Ball and stick 8

1.2.4 NODDI 8

1.3 Diffusion MRI phantoms 9

1.3.1 Diffusion MRI phantom requirements 11

1.3.2 Existing Phantoms 12

1.4 Thesis Outline 14

2 Validation of a 3D printed phantom for diffusion MRI 16

2.1 Introduction 16

2.2 Materials and methods 19

2.2.1 Phantom preparation 19

2.2.2 Microscopy 19

2.2.3 Synchrotron phase contrast micro-CT 21

2.2.4 MRI scanning and model fitting 21

2.2.5 Phantoms for assessing the reproducibility of dMRI metrics 22

2.2.6 Phantoms for assessing stability over time and the effect of print parameters on dMRI 22

2.3 Results 23

2.3.1 Microscopy 23

2.3.2 Micro-CT 24

2.3.3 Nominal phantom characteristics and reproducibility 24

2.3.4 Metric variation with print parameters 26

2.3.5 Metric stability over time 27

2.4 Discussion 27

2.4.1 Phantom vs. human microstructural fibre geometry 27

2.4.2 Phantom vs. human diffusion characteristics 28

2.4.3 Phantom reproducibility and stability 30

2.4.4 Method advantages 31

2.5 Conclusion 32

3 Characterization of fibre geometry's effect on diffusion MRI models 33

3.1 Introduction 33

3.2 Methods 34

3.3 Results . . . 37
3.3.1 DTI . . . 38
3.3.2 DKI . . . 40
3.3.3 Ball and Stick . . . 42
3.3.4 NODDI . . . 42
3.3.5 Bingham-NODDI . . . 44
3.4 Discussion . . . 45
3.4.1 DTI . . . 46
3.4.2 DKI . . . 46
3.4.3 Ball and stick . . . 47
3.4.4 NODDI . . . 47
3.4.5 Bingham-NODDI . . . 48
3.4.6 Phantom performance . . . 48
3.4.7 Model Performance . . . 49
3.5 Conclusions . . . 50

4 Conclusions **52**
4.1 Future work . . . 55

Bibliography **56**

A 3AM Phantom Production Protocol **63**

B Copyright Permission **66**

Curriculum Vitae **69**

List of Figures

1.1 An illustration of proton precession forming bulk magnetization. From reference [1] with permission from John Wiley and Sons. (a) Protons have spin, generating a magnetic field that tends to align with the B_0 field. (b) If tipped away from the B_0 field with an RF pulse, a proton will precess at the Larmor frequency ω. (c) In a group of protons in a B_0 field, more will align with the field than against it, generating a bulk magnetization that will precess at the Larmor frequency if tipped away from the B_0 field. 3

1.2 The radio frequency and diffusion gradient pulses used in the pulsed gradient spin echo sequence. Adapted from reference [2], with permission under the Creative Commons Attribution License. 4

1.3 Probability plots for the Bingham and Watson distributions. Adapted from Reference [13], with permission under the Creative Commons Attribution License. (a) Isotropic dispersion about the central orientation, which can be modeled with the Watson or Bingham distributions. (b) Anisotropic dispersion about the central orientation, which can only be modeled by the Bingham distribution. (c) Maximally anisotropic dispersion about the central orientation, which can only be modeled by the Bingham distribution. 9

2.1 Schematic and photographs of 3AM phantoms. (a) PVA dissolves away when placed in water leaving microporous structure. (b) 3AM phantom before dissolving. (c) 3AM phantom after dissolving. (d) Dissolved 3AM phantoms stacked in a test tube with water that are ready for imaging. 20

2.2 Microscopy images of 3AM phantoms. (a) Confocal microscopy z-stack image of a stained cross sectional phantom sample, averaged across slices. Elastomeric matrix (red) and pores (black) are visible. The white outline indicates individual lines of material. (b) 2D projection of a 3D microscopy volume acquired with confocal microscopy. Regions shown in red are the matrix of the 3AM phantom that is composed of elastomer while the black regions are pores. Outlined in yellow are larger pores caused by the printing pattern of the phantom. In both a and b, the image plane is perpendicular to the long axis of the pores. 24

2.3 Pore segmentation results. (a-c) Confocal microscopy image before (left) and after (right) performing pore segmentation. (d) normalized histogram of equivalent diameter of pores obtained from segmentations in a-c and their frequencies (Total N = 1912). 25

2.4 Synchrotron micro-CT scan data at two zoom levels, transformed to align lines of material with the viewing planes. Upper row: View of the entire scan ROI. Lower row: Detailed view of a short length of five stacked lines of material. The direction of print-head motion was left-right in the left- and right-most columns, and perpendicular to the image in the center column. 26

2.5 Expected signal vs. b-value from the DKI fit in: (a) the axial direction, and (b) the radial directions. 27

2.6 FA, diffusivities, and kurtosis of phantoms printed with different printing parameters. (a-c) DKI metrics vs. printing temperature. (d-f) DKI metrics vs. printing speed. (g-i) DKI metrics vs. layer thickness. (j-l) DKI metrics vs. infill density. 28

2.7 DKI metric stability in a nominal phantom over 76 days. (a) FA. (b) Diffusivities. (c) Kurtosis. 29

3.1 The five phantom patterns, with alternating layers superimposed on one another, and a demonstration of the phantoms' scale. (a) Bending. (b) Straight. (c) Kissing. (d) Fanning. (e) Crossing. (f) The fanning phantom with a magnified view including the 0.7 mm isotropic in-plane voxel size superimposed. . . 36

3.2 A summary of the results. From left to right, the columns correspond to the bending, straight, kissing, fanning, and crossing phantoms. The top row shows the schematic of each phantom, the second row shows an image of each phantom without diffusion weighting, the third row shows the ground truth description registered to image space, and the fourth row shows the DTI-derived FA map of each phantom as an example. 38

3.3 DTI metrics vs. orientation dispersion metrics in each of the four phantoms. Each row depicts the relationship between one metric and orientation dispersion, and each column depicts the data from one or two phantoms. From left to right, those phantoms are: bending, straight, fanning and kissing, and crossing. . 39

3.4 DKI kurtosis metrics vs. orientation dispersion metrics in each of the four phantoms. Each row depicts the relationship between one metric and orientation dispersion, and each column depicts the data from one or two phantoms. From left to right, those phantoms are: bending, straight, fanning and kissing, and crossing. 41

3.5 Ball and stick volume fractions vs. orientation dispersion metrics in each of the four phantoms. Each row depicts the relationship between one metric and orientation dispersion, and each column depicts the data from one or two phantoms. From left to right, those phantoms are: bending, straight, fanning and kissing, and crossing. 42

3.6 NODDI metrics vs. orientation dispersion metrics in each of the four phantoms. Each row depicts the relationship between one metric and orientation dispersion, and each column depicts the data from one or two phantoms. From left to right, those phantoms are: bending, straight, fanning and kissing, and crossing. . 43

3.7 Bingham-NODDI metrics vs. orientation dispersion metrics in each of the four phantoms. Each row depicts the relationship between one metric and orientation dispersion, and each column depicts the data from one or two phantoms. From left to right, those phantoms are: bending, straight, fanning and kissing, and crossing. 44

List of Tables

2.1 The parameters used to print the phantoms 23

2.2 Mean dMRI metrics from four phantoms and their coefficient of variation. . . . 27

3.1 The phantom fibre configurations. 35

A.1 Nominal phantom printing parameters 65

List of Abbreviations and Symbols

Abbreviations

3AM	3D printed axon-mimetic
AD	Axial diffusivity
AK	Axial kurtosis
CSF	Cerebrospinal fluid
CT	Computed tomography
dMRI	Diffusion magnetic resonance imaging
DKI	Diffusion kurtosis imaging
DTI	Diffusion tensor imaging
DWI	Diffusion-weighted image
ETL	Echo train length
FA	Fractional anisotropy
FDM	Fused deposition modeling
FOV	Field of view
MD	Mean diffusivity
MDT	Microstructure diffusion toolbox
Micro-CT	Micro-computed tomography
MK	Mean kurtosis
MRI	Magnetic resonance imaging
NODDI	Neurite orientation dispersion and density imaging
ODI	Orientation dispersion index
ODI_P	Primary orientation dispersion index
ODI_S	Secondary orientation dispersion index
PGSE	Pulsed gradient spin echo
PVA	Polyvinyl alcohol
RARE	Rapid acquisition relaxation enhancement
MSME	Multi-slice-multi-echo
RD	Radial diffusivity
RK	Radial kurtosis
RF	Radio frequency
SE	Spin echo
SNR	Signal to noise ratio
TE	Echo time
TR	Repetition time

Symbols

b	b-value; diffusion weighting
B_0	Static magnetic field used in MRI
D	Diffusivity
D	Diffusion tensor
$\hat{g}$	Direction-encoding vector
G	Gradient amplitude
K	Kurtosis
S	Signal
S_0	Signal with no diffusion weighting
δ	Gradient pulse duration
Δ	Gradient pulse interval
λ	Diffusion tensor eigenvalue
γ	Gyromagnetic ratio
ω	Larmor frequency

Chapter 1

Introduction

The brain is one of the most important organs of the human body, but it is also poorly understood. A "comprehensive structural description of the network of elements and connections forming the human brain", referred to as the human connectome [3], would be an immensely useful tool to advance the understanding of the brain's function in sickness and health. Developing a non-invasive imaging modality capable of precisely resolving and accurately characterizing individual neurons or neural pathways is a critical step in the process of assembling the human connectome. Furthermore, an understanding of how neuronal structure changes in pathology may help understand and treat that pathology. Standard magnetic resonance imaging (MRI) produces more detailed images of the brain than any other conventional modality, but its nominal resolution of about one millimetre is much too coarse to track individual neurons, which typically have sizes on the scale of micrometres. [4]

1.1 Diffusion MRI

Diffusion MRI (dMRI) is a technique that addresses the coarse resolution of standard MRI by using an MRI sequence that is sensitive to the diffusion of water molecules in the brain. [4] Axons, the neural structures that form the pathways that connect multiple neurons in the brain, have a tube-like structure that can hinder or restrict diffusion perpendicular to their path. Re-

stricted diffusion refers to a situation in which the diffusion of water molecules is obstructed by a barrier that cannot be passed by taking another path, as is the case within axons. Hindered diffusion refers to a situation in which the diffusion of water molecules is obstructed by barriers that can be bypassed by an indirect path, as is the case between axons in a bundle. Diffusion MRI signal reflects these patterns of diffusion within voxels, providing microstructural information that is not available from standard structural MRI.

Diffusion MRI is conducted with a standard MR scanner, which applies a constant magnetic field (B_0) along the bore of the scanner. When a subject is placed in a scanner, the magnetic fields of protons (hydrogen atoms) in the subject tend to align with the static field produced by the scanner [1]. This tendency of individual protons to align their magnetization with the B_0 field produces a bulk magnetization aligned with the B_0 field. If the magnetization of the protons is tipped out of alignment with the B_0 field, the bulk magnetization will precess around the B_0 field, spiraling about the field until it returns to alignment, as illustrated in Figure 1.1. The frequency of this precession is known as the Larmor frequency ω, and is determined by the product of the strength of the field, B_0, and a constant γ called the gyromagnetic ratio. As an equation:

$$\omega = \gamma B_0. \tag{1.1}$$

The standard structural MRI sequence used to produce structural images is known as a spin echo (SE) sequence. A spin echo sequence works by applying radio frequency (RF) pulses to the subject, tuned to the Larmor frequency, that allow the bulk magnetization of the subject's protons to be tipped away from the B_0 field. In each cycle of a spin echo sequence, a 90° pulse is applied to tip the magnetization perpendicular to the B_0 field, then a 180° pulse is applied shortly after. In the time between the 90° pulse and the 180° pulse, the spins that produce the bulk magnetization dephase due to local variations in the magnetic field. The same amount of time after the 180° pulse, the spins come back into phase, producing an echo of the signal produced by the 90° pulse, as illustrated in the top row of Figure 1.2. The amount of time

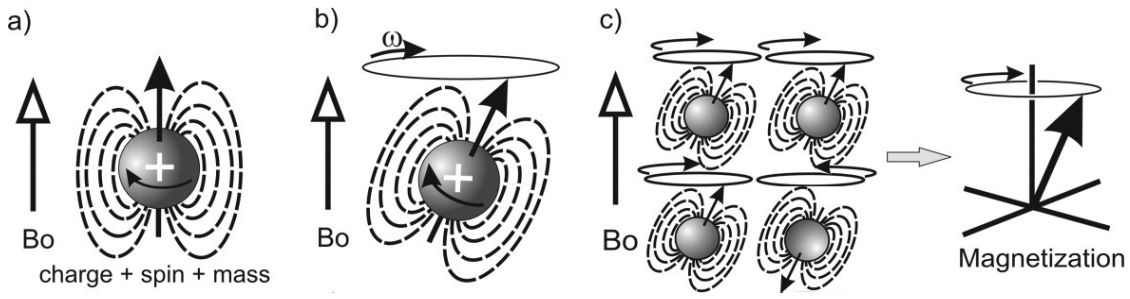

Figure 1.1: An illustration of proton precession forming bulk magnetization. From reference [1] with permission from John Wiley and Sons. (a) Protons have spin, generating a magnetic field that is more likely to to align with the B_0 field than in any other direction. (b) If tipped away from the B_0 field with an RF pulse, a proton will precess at the Larmor frequency ω. (c) In a group of protons in a B_0 field, more will align with the field than against it, generating a bulk magnetization that will precess at the Larmor frequency if tipped away from the B_0 field.

between the 90° pulse and the echo is the echo time (TE), and the amount of time between successive 90° pulses is the repetition time (TR). This echo becomes the signal which forms the MR image, and SE sequences can be tuned to be sensitive to different relaxation times, which characterize the process by which the bulk magnetization returns to alignment with the B_0 field. These relaxation times form the basis of standard structural MRI.

To achieve diffusion weighted MR signal, spin echo sequences are extended to pulsed gradient spin echo (PGSE) sequences. In PGSE, a gradient that modulates the B_0 field along a single direction is applied before the 180° pulse, and another gradient with the same polarity is applied after the 180° pulse, as illustrated in Figure 1.2. The first gradient pulse causes precession of protons along the specified direction to dephase. The second gradient pulse has the opposite effect due to the 180° pulse, rephasing the precession of those protons. However, protons in water naturally diffuse, or randomly move, including along the direction specified by the gradient pulses. Any protons that diffused along that direction end up out of phase, reducing the measured signal relative to what it would have been without the gradient pulses. Effectively, this weights the corresponding PGSE acquisition according to the direction and strength of the gradient pulses.

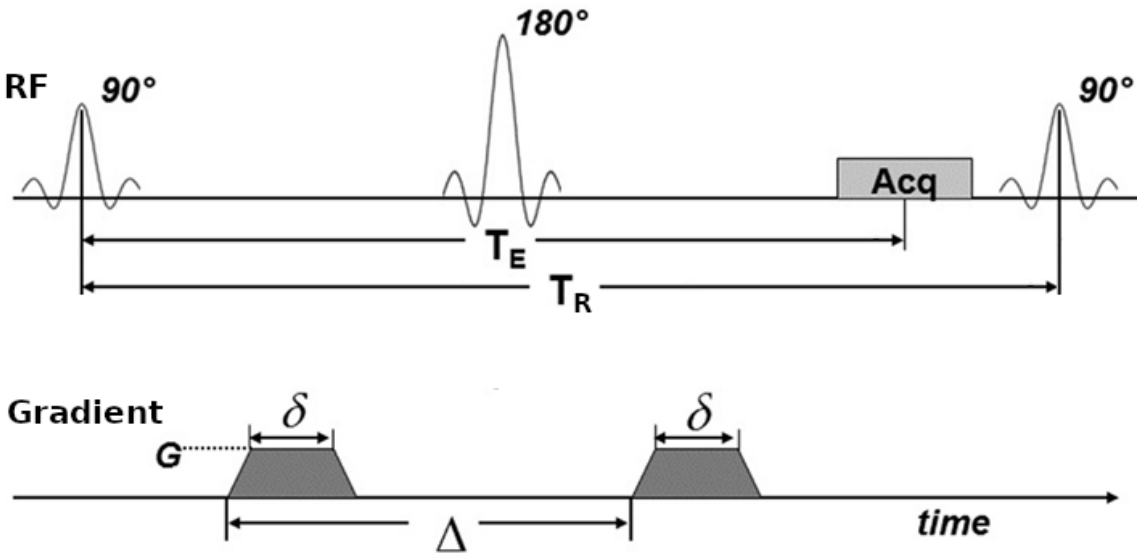

Figure 1.2: The radio frequency and diffusion gradient pulses used in the pulsed gradient spin echo sequence. Adapted from reference [2], with permission under the Creative Commons Attribution License.

The strength of the diffusion weighting depends on the gyromagnetic ratio (γ), the magnitude (G) and duration (δ) of the gradient pulses, and the time interval between the two gradient pulses (Δ). Put together, these factors produce the b-value, which reflects the overall diffusion weighting of a given PGSE acquisition. The b-value is measured in $\mathrm{s/mm^2}$ and is defined as follows:

$$b = \gamma^2 G^2 \delta^2 (\Delta - \delta/3). \tag{1.2}$$

The diffusion behaviour of a uniform, isotropic medium can be summarized with a single metric, its diffusivity (D), measured in $\mathrm{mm^2/s}$. Given this diffusivity, the signal S measured from a diffusion-weighted scan with b-value b of a region can be related to the signal from an identical acquisition with no diffusion weighting (S_0), by the following equation:

$$S = S_0 e^{-bD} \tag{1.3}$$

To accurately characterize non-isotropic media like tissue with dMRI, multiple diffusion-

weighted images (DWI) can be generated by repeating this PGSE process several times with different gradient directions and b-values. [5] The resulting dMRI scan data are 4-dimensional, where the first three dimensions are spatial, and each element in the fourth dimension corresponds to a volume with a single gradient direction and b-value. A set of DWIs of a subject therefore reflect the complex diffusion behaviour within each voxel of that and is a rich source of information, but requires analysis and simplification to interpret.

1.2 Diffusion MRI models of white matter

An ongoing challenge in diffusion MRI is to develop a model that accurately describes the received dMRI signal in terms of the underlying brain physiology. A set of DWIs of a subject contains data that reflects the subject's diffusion behaviour, but each spatial voxel has a set of values, each associated with one of the dMRI acquisitions. This multiplicity of data makes it difficult for a human to analyze a set of DWIs as a whole and draw accurate conclusions about the underlying microstructure. Instead, we can apply an understanding of diffusion MRI to mathematically represent the data in a more compact and apparently meaningful form. Further, we can apply a theory of the subject's microstructure to build a model that explicitly represents the dMRI signal in terms of that microstructure [6]. Such a model that successfully describes brain microstructure would enhance the clinical utility of dMRI.

Once a mathematical signal representation or model is described, it is applied to a dataset, typically at a voxel-wise level, by finding the parameters of the representation that best describe the signal at each voxel. This is an optimization problem, where the goal is to minimize the error between the signal predicted by the representation and the measured signal. This process is called "fitting" the model to the data. The method used to fit a given model to a dataset depends on the form of the model. For relatively simple or fundamental representations, the model fit can be posed as a linear system of equations, allowing an optimal fit to be found in closed form using the linear least squares method. To fit more complex representations, including most mi-

crostructural models, a nonlinear optimization procedure is required [7]. Typically, nonlinear optimization procedures have no closed-form solution and are computationally intensive, so fitting more complex representations can result in less precise results and can take longer than simpler representations.

1.2.1 Diffusion tensor imaging

Diffusion Tensor Imaging (DTI) is a simple, widely used dMRI signal representation. DTI extends the model of signal attenuation in an isotropic medium ($S/S_0 = e^{-bD}$) by replacing the single diffusivity D with 3×3 diffusion tensor $\mathbf{D}$, which allows anisotropic diffusion [8]. DTI relates the applied gradients to the signal attenuation observed in each acquisition by the following equation:

$$S/S_0 = e^{-b\hat{g}^T \mathbf{D} \hat{g}} \tag{1.4}$$

where $\hat{g}$ is a unit vector that encodes the direction of the applied diffusion gradient. The diffusion tensor is symmetric, so it has seven independent parameters to estimate. By observing $\ln(S/S_0) = -b\hat{g}^T \mathbf{D} \hat{g}$ is a linear system of equations, we see that we can fit DTI using a linear least squares method. To summarize the diffusion pattern described by DTI, we can find the eigenvalues and eigenvectors of the diffusion tensor by diagonalizing the 3×3 matrix that forms the tensor. Each eigenvalue corresponds to the estimated diffusivity in one of three perpendicular directions, and each eigenvector indicates the principal direction associated with its corresponding eigenvalue.

Four metrics are typically extracted from DTI. Axial diffusivity (AD) is simply the largest eigenvalue, and describes the diffusivity along a primary axis of diffusion. Radial diffusivity is the mean of the two smaller eigenvalues, and indicates the tendency of water to diffuse perpendicular to the central axis of diffusion. Mean diffusivity (MD) is the mean of the three eigenvalues, and indicates the overall ability of water to diffuse in a voxel. Finally, fractional

anisotropy (FA) is a metric that indicates the tendency of water to diffuse along one central axis, rather than diffuse isotropically. FA is defined by:

$$FA = \sqrt{\frac{3((\lambda_1 - MD)^2 + (\lambda_2 - MD)^2 + (\lambda_3 - MD)^2)}{2(\lambda_1^2 + \lambda_2^2 + \lambda_3^2)}}, \tag{1.5}$$

where λ_1, λ_2, and λ_3 are the three eigenvalues of the diffusion tensor. FA is measured from zero to one, where an FA of zero indicates perfectly isotropic diffusion, and an FA of one indicates diffusion only in one direction.

1.2.2 Diffusion kurtosis imaging

DTI and metrics derived from it have been applied clinically, but it breaks down in voxels where multiple fibres interact and when a high diffusion weighting is used in a scan. [6] Diffusion Kurtosis Imaging (DKI) extends DTI to describe non-Gaussian diffusion patterns [9, 10], which are typically observed when high diffusion weightings are used in non-homogeneous environments, like human white matter. To quantify non-Gaussian diffusion, DKI adds a kurtosis term to the one-dimensional diffusion described by Equation 1.3:

$$\ln(S/S_0) = -bD + \frac{1}{6}b^2D^2K, \tag{1.6}$$

where K is the diffusional kurtosis [9], which describes the degree of deviation from free Gaussian diffusion. Like DTI, DKI extends this equation into 3D by forming a kurtosis tensor. The kurtosis tensor is a symmetric $3\times3\times3\times3$ tensor, with 15 independent elements. The DKI representation also forms a system of linear equations that can be solved with a linear least squares method, but requires a dataset with more acquisitions than are necessary for DTI, and requires some of those acquisitions to have a higher b-value than that necessary for DTI.

In addition to the four DTI metrics, DKI adds three analogous metrics that describe the directional kurtosis in a voxel. Axial and radial kurtosis (AK and RK) describe the kurtosis of the diffusion pattern along and perpendicular to the central axis of diffusion, respectively.

Mean kurtosis (MK) describes the overall amount of kurtosis in a voxel.

1.2.3 Ball and stick

The ball and stick representation is one of the simplest compartment-based representations of dMRI signal [11]. It decomposes dMRI signal into two compartments: the "ball" compartment, which contains isotropically diffusing water with the same diffusion behaviour described by Equation 1.3, and the "stick" compartment, which is composed of a zero-radius cylinder that only allows diffusion in one direction. The parameters of the model are then the diffusivity of the two compartments, the volume fraction of one of the compartments, and the direction in which the stick compartment is oriented. Depending on the application, some of the parameters (typically the diffusivities) may be fixed before the model fit, making an assumption of a typical value to increase the stability of the fit.

1.2.4 NODDI

Neurite orientation dispersion and density imaging (NODDI) [12] is another compartment model that includes three compartments: intra-axonal space, extra-axonal space, and CSF. The CSF compartment is represented as isotropic diffusion, exactly like the ball compartment in the ball and stick model. The intra- and extra-axonal space are represented as distributions of fibres, rather than one or more individual fibre populations, each oriented in its own direction, like the stick compartment in the ball and stick model. NODDI uses the Watson distribution, which describes an isotropically decreasing orientation density about a mean orientation on the unit sphere, to model its fibres. The intra-axonal space is represented by a Watson distribution of zero-radius cylinders, and the extra-axonal space is represented by a Watson distribution of cyclindrically symmetric diffusion tensors.

NODDI fixes the assumed diffusivities of each of its compartments to biologically plausible values, leaving five parameters to be estimated in each voxel: the intra-cellular and isotropic volume fractions, two direction parameters to specify the mean orientation, and the concentra-

tion parameter of the Watson distribution, which specifies how broad the distribution is. The concentration parameter is usually mathematically transformed to an orientation dispersion index (ODI), which describes the amount of orientation dispersion from zero to one. NODDI's parameter set therefore aims to describe both the microstructure and orientation of the neurites in a given voxel.

Bingham-NODDI [13] is a variant of NODDI that uses the Bingham distribution instead of the Watson distribution, as illustrated by Figure 1.3. The Bingham distribution allows a different amount of dispersion in perpendicular directions relative to the mean orientation. Instead of a single ODI like NODDI, Bingham NODDI has a primary ODI (ODI_P) and a secondary ODI (ODI_S). Practically, this allows Bingham-NODDI to represent patterns of diffusion that NODDI struggles with, in particular patterns where diffusion is limited to a single plane.

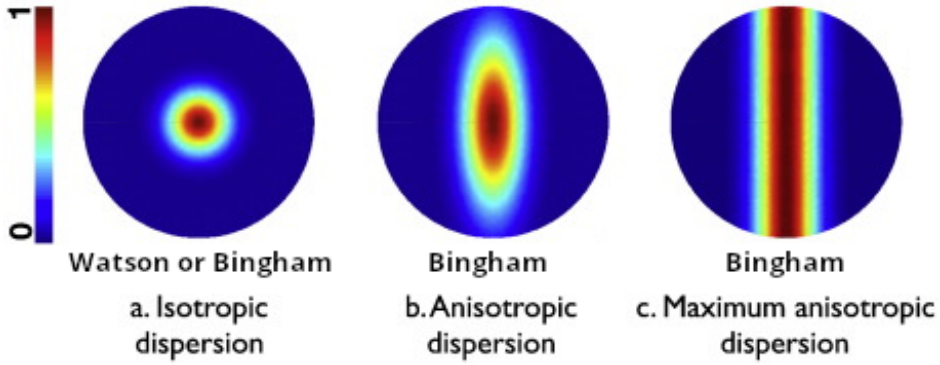

Figure 1.3: Probability plots for the Bingham and Watson distributions. Adapted from Reference [13], with permission under the Creative Commons Attribution License. (a) Isotropic dispersion about the central orientation, which can be modeled with the Watson or Bingham distributions. (b) Anisotropic dispersion about the central orientation, which can only be modeled by the Bingham distribution. (c) Maximally anisotropic dispersion about the central orientation, which can only be modeled by the Bingham distribution.

1.3 Diffusion MRI phantoms

The wealth of available models offers the ability to estimate many quantitative characteristics of the brain, but a major obstacle to the widespread adoption of any model in the research and

clinical communities is a lack of evidence that they accurately estimate a given quantity [14]. Diffusion MRI is the only imaging modality that can safely make these microstructural predictions on a living human, so there is no "ground truth" value to compare with each estimation.

To obtain this ground truth, parameter estimates from dMRI scans of animals can be compared to ex vivo histology of the same animals. The major advantage of this approach to validating dMRI models of white matter is that all the data comes from brain tissue, so it is as realistic as possible. However, brain tissue changes as it is prepared for histology, and in particular has been observed to shrink as it is prepared, so the correspondence between the histological ground truth and the scan data is not guaranteed to be perfectly valid. [15] Furthermore, control of fibre orientation in the sample is limited to choosing areas of interest, unlike synthetic samples that can be designed to answer a specific question about a dMRI model.

Another common technique for diffusion MRI model validation is the use of Monte Carlo simulations of axonal fibres, also referred to as numerical phantoms. The primary advantage of numerical phantoms is that they allow fine-grained control and precise understanding of the tissue properties and diffusion behaviour under investigation, so they can be used to answer specific questions about a dMRI model's response to a well-understood sample with a very precise ground truth. However, the synthetic nature of the data means that its fidelity depends on an accurate model of both the sample in question and dMRI scanning procedure to produce accurate data. It is difficult to capture all of the involved complexity, so numerical phantoms often use relatively simple models of straight cylinders as the sample, and struggle to capture scanning complexities like inhomogeneity in the static magnetic field. Finally, performing the involved simulation can be computationally expensive, especially as the involved models increase in complexity and realism. [16]

Instead of histology or numerical phantoms, physical phantoms can be used to provide a ground truth for validation of diffusion MRI models. A physical phantom is a synthetic object designed to mimic the dMRI characteristics of the brain when used as a dMRI subject. By undergoing dMRI scans, physical phantoms offer data that incorporate the complexities

inherent to a diffusion MRI scan, unlike synthetic phantoms. Physical phantoms are also more easily characterizable by complementary imaging modalities than living tissue. Like numerical phantoms, but less completely, some properties of physical phantoms can be controlled when they are designed, tuning a phantom to answer a specific question. To characterize uncontrolled microstructural properties, a physical phantom can be imaged by modalities like micro-CT without being damaged by the high dose of ionizing radiation required. Physical phantoms offer more control over the ground truth than tissue samples, but less than numerical phantoms. Physical phantoms typically offer more realistic scan data than numerical phantoms, but less realistic scan data than tissue samples.

1.3.1 Diffusion MRI phantom requirements

To accurately mimic the microstructure of white matter, dMRI phantoms contain an MR-visible liquid (often water) and solid fibrous structures that hinder or restrict the diffusion of that liquid. [16] The fibres must have a similar scale and configuration to the neurons in the brain to modulate diffusion in a way that produces a realistic dMRI signal. Beyond accurately mimicking white matter's diffusion behaviour, dMRI phantoms should be convenient to manufacture and produce consistent data when scanned at different times or on different hardware.

Axonal fibres in the brain have very small diameters, typically from 0.5 μm to 1 μm [17], that are arranged in complex configurations. In designing a physical phantom, both of these properties of axonal fibres are difficult to mimic, and it is even more difficult to mimic both in the same phantom. To quantify the extent to which a phantom meets these fundamental requirements, the inner and outer diameters, as applicable, of its fibrous structures can be measured with a non-dMRI modality. A dMRI phantom should also be able to represent as many types of complex orientations as possible. Tournier et al. identify four types of complex orientations [18]: bending fibres, fanning fibres, interdigitating fibres, and adjacent fibres. An ideal phantom would be able to reproduce all four of these fibre configurations.

A dMRI phantom that successfully mimics the microstructure of the brain should also

produce similar dMRI signal to that produced by the brain. To assess the similarity of signal from a phantom and signal from the brain, a widely-used signal representation should be fit to the data, allowing the metrics to be compared. DTI and DKI are both widely used and stable in their fit, so they work well for this purpose. To minimize the effect of orientation dispersion, a straight region of a phantom should be compared to a straight region of the brain. FA is a particularly relevant metric for this purpose because the hindering and restriction of diffusion in white matter tracts tends to produce highly anisotropic diffusion. [19] However, the error in all DTI and DKI metrics are useful to indicate differences in diffusion between a phantom and the brain, and together they provide a good set of summary statistics for validating a phantom.

To assess how consistent the data a phantom produces is, several specifications can be taken into account. First, the phantoms should be manufactured reproducibly, so the coefficient of variation in mean FA of any five phantoms manufactured under the same conditions should be as low as possible. Second, the phantoms should be stable over time, so it should take as long as possible for the percent change in FA of a single phantom to exceed 5%. [20] Finally, susceptibility differences between the liquid and solid in a phantom should be as low as possible to minimize artifacts.

To assess how convenient a phantom is to produce, the cost and time to manufacture it should be measured. Both the one-time cost of equipment and the recurring cost of materials to produce a single phantom should be minimized. The total time to manufacture a phantom should also be minimized. These metrics are not widely reported in the literature, but are of practical importance to researchers who would like to perform a phantom validation of a dMRI model of white matter.

1.3.2 Existing Phantoms

A wide range of materials have been used to produce the fibrous structures required by a dMRI phantom. Existing phantoms use rigid capillaries, glass capillary arrays, two types of hollow fibres, and several classes of plain fibres. Each type of phantom makes trade-offs to serve a

specific purpose and fulfills the general requirements for dMRI phantoms to a different extent.

Phantoms made with rigid capillaries use capillaries with micrometre-scale inner diameters, typically made from glass, to anisotropically restrict diffusion within the cylinders and hinder diffusion between the cylinders. The primary benefit of these phantoms is that they can be manufactured at very small sizes while representing both intra- and extracellular space. The primary drawback of rigid capillaries is that their rigidity makes it difficult to produce phantoms with complex orientations; the most complex orientation that has been demonstrated with this type of phantom is layers representing interdigitating fibres. [21]

Glass capillary arrays are small wafers of glass with holes that act as capillaries, restricting water diffusion. [22, 23] Like glass capillaries, the holes in glass capillary arrays are straight, limiting the orientational complexity they can achieve. Their primary application has been evaluating diffusion MRI models that estimate axon diameters. Only the spaces within the capillaries contain water, so only intracellular diffusion is represented by these phantoms.

Hollow fibres are flexible and polymeric, representing intra- and extracellular space when packed densely enough. Two techniques have been reported for manufacturing hollow fibres for diffusion MRI phantoms: melt-spinning extrusion [24] and coaxial electrospinning. [25] Melt-spinning extrusion works by melting polypropylene chips and extruding the molten polymer through C-shaped dies to form hollow fibres with diameters on the order of 12 μm. The resulting fibres have been packed tightly enough to achieve a very high FA but have higher diameters than electrospun fibres. Electrospinning works by applying a high voltage between a needle filled with a liquid polymer and a flat collector some distance away. The buildup of charge in the liquid forces it to erupt from the needle in a jet and hit the collector. A variant of this procedure that uses two coaxial needles [26] can be used to create membranes of hollow fibres with customizable and small diameters.

Other phantoms use plain (i.e. not hollow) fibres, packed tightly to hinder diffusion, representing only extra-axonal space. Dyneema, a polymeric fibre with favourable magnetic susceptibility, has been identified as a useful material for this purpose. [20] The primary difference

between different types of plain fibre phantoms is the fixation method that determines the geometry of each phantom. Shrink tubes [27, 28] compressing bundles of fibres have been shown to be effective, and capable of representing crossing fibres. However, the fibre density of plain fibres in shrink tubes is difficult to precisely control. Winding plain fibres around a spindle is an effective way to pack fibres very densely, and arranges fibres in a bending pattern [29]. Finally, winding plain fibres around a custom 3D printed support with sections that produce different fibre densities and orientations has been shown to be a useful, if labour-intensive, technique [30].

1.4 Thesis Outline

Existing dMRI phantoms trade off between cost and ease of use, microstructural similarity to white matter, and orientational complexity. Their costs and ease of use are not consistently reported, but none are both easily produced and able to produce complex orientations. A phantom that filled this niche would be a practical tool for assessing the response of dMRI models of white matter to orientational complexity.

This thesis considers a 3D printed axon-mimetic (3AM) diffusion MRI phantom that is produced by fused deposition modeling (FDM) 3D printing with an experimental filament [31]. The filament consists of an elastomeric matrix filled with pockets of polyvinyl alcohol (PVA). When the 3D printer melts the filament and extrudes it into narrow lines, the pockets of PVA stretch into fibres along the direction of motion of the print head. If a phantom composed of layers of these lines is immersed in water, the PVA fibres dissolve, leaving behind fibrous pores that modulate diffusion anisotropically, forming the fibrous structures necessary for a dMRI phantom to mimic the diffusion behaviour of axonal fibres. Conventional 3D printers are inexpensive, easy to use, and highly configurable, and the material used to produce 3AM phantoms is also inexpensive. Therefore, 3AM phantoms have the potential to be a useful tool for validating diffusion MRI models of white matter. The first objective of this thesis is

to characterize 3AM phantoms according to the requirements laid out above, validating them as appropriate for use as dMRI phantoms. The second objective of this thesis is to use a set of dMRI phantoms to characterize the effect of orientation dispersion on a set of dMRI representations and models of white matter, demonstrating their utility.

Chapter 1 presented diffusion MRI as an imaging modality, introduced dMRI modeling techniques and some common dMRI signal representations, and described the requirements of dMRI phantom with a survey of existing dMRI phantoms.

Chapter 2 presents a characterization of the microstructural and diffusion characteristics of 3AM phantoms. The objective of the Chapter is to validate 3AM phantoms' appropriateness and effectiveness for use in validating diffusion MRI models of white matter. A version of this Chapter entitled "Microstructural characterization and validation of a 3D printed phantom for diffusion MRI" was submitted for publication in Magnetic Resonance in Medicine in July 2020.

Chapter 3 presents the characterization of the response of diffusion MRI models of white matter to fibre curvature and crossing fibres using a set of 3AM phantoms with complex fibre configurations.

Chapter 4 summarizes the contributions and limitations of this project, and lays out potential future steps for the project.

Chapter 2

Validation of a 3D printed phantom for diffusion MRI

2.1 Introduction

Diffusion magnetic resonance imaging (dMRI) produces images by sensitizing the MRI signal to the random motion of water molecules on a micrometre scale. This sensitivity means that dMRI signal reflects patterns of water diffusion in the brain imposed by brain microstructure. To interpretat of dMRI signal, signal representations like diffusion kurtosis imaging (DKI) [32] have been developed. By fitting raw dMRI data to mathematical representations whose parameters describe general features of the underlying diffusion, this technique produces metrics that are related to the microstructure and structural connectivity of the brain [32]. However, a limitation of this approach to characterizing brain microstructure is that there is typically no in-vivo ground truth to validate the findings of a given study.

A number of techniques have been used to produce data for the validation of dMRI models, including numerical phantoms [33, 34], ex-vivo brain samples [35, 36], in-vivo studies [37], and physical phantoms [22, 38]. Numerical phantoms are simulations of diffusion behaviour under explicitly defined conditions and geometries. They allow precise experimental control,

but do not reproduce all the complexity inherent to a real scan. Ex-vivo studies are performed by imaging animal brains in vivo, then sacrificing animals and analysing histological sections of the animals' brains to validate the findings of the imaging study [39]. These methods provide data directly from a real brain, but histology is a time-consuming and costly approach that covers a limited region of interest in the brain that is difficult to register to a dMRI scan. Further, there may be microstructural changes in the tissue due to histological preparation/fixation. Physical phantoms are artificial objects designed to mimic the diffusion characteristics of the brain, producing dMRI scan data similar to that seen from real brains. Physical phantoms occupy a middle ground between the two ends of a spectrum defined by numerical and ex-vivo studies: they produce real scan data with a well-known microstructural ground truth, but are not as customizable as numerical phantoms or as true to the structure of the brain as ex-vivo samples.

Several types of physical phantoms have been previously proposed. Glass capillaries [40] provide reliably anisotropic diffusion in a pattern that is straightforward to characterize, but cannot mimic some complex geometric fibre configurations that are observed in the brain. Straight fibres can be produced with axon-scale diameters to mimic hindered diffusion between axons, but are difficult to arrange with the geometric complexity of some brain regions. Extruded or electrospun hollow fibers [41] mimic axonal diffusion patterns well, but are expensive and time-consuming to produce. As such, the development of dMRI phantoms involves trade-offs between the cost of materials and equipment, ease of production, the ability to achieve accurate brain-mimetic microstructure, and geometric complexity. Using existing procedures to produce a physical phantom with biologically plausible microstructure and geometric complexity is expensive and time-consuming, so an alternative that is both adequately brain-mimetic and easy to produce is needed.

Fused Deposition Modeling (FDM) 3D printing is an inexpensive and flexible manufacturing technique that enables repeatable production of custom parts. FDM works by melting a polymeric filament and depositing the molten material one line at a time in a sequence of

layers. FDM can control the physical properties of printed objects by changing parameters like the temperature of the print head and speed at which material is deposed. It also allows the within-layer print path to be designed to adjust the overall material properties of the finished product. Given the flexibility and low cost of FDM, it would be advantageous to apply it to the production of physical dMRI phantoms.

For the FDM production of 3D-printed Axon Mimetic (3AM) phantoms, we propose the use of a dual component "porous filament" material [31]. In this work, we utilized "GEL-LAY" (LAY Filaments, Cologne, Germany), which is composed of an elastomeric matrix infused with pockets of polyvinyl alcohol (PVA). When 3D printed, the PVA forms long fibres within each line of printed composite material. PVA is water-soluble, so when this 3D printed material is immersed in water, the PVA fibres dissolve, leaving behind microscopic fibrous pores, as illustrated in Figure 2.1a. The anisotropic structure of these fibrous pores mimic the anisotropic shape of axonal fibres and modulate diffusion in a similar way, allowing 3D printed porous filaments to form the basis of a phantom that can validate dMRI [42].

For 3AM phantoms to be useful, their pores' size should be as close as possible to axon diameters seen in the human brain, which are typically on the order of 0.5 μm to 1 μm. Furthermore, the pores' orientations must be well-known and should be controllable. The overall T1 and T2 relaxation times modulate the achievable SNR in a scan of the phantoms [16], so phantom materials should shorten relaxation times as little as possible. A dMRI scan of a 3AM phantom should show diffusion characteristics as similar to those seen in the human white matter as possible. Any dependence of those diffusion characteristics on 3D print parameters should be identified to facilitate customization of individual phantoms. Finally, 3AM phantoms' diffusion characteristics should be consistent from print to print and should be as stable as possible over time.

In this study, we use both fluorescent microscopy and synchrotron phase-contrast micro-computed tomography, a novel technique that allows exceptionally fine-resolution 3D visualization of soft structures, to characterize and visualize the microstructure of 3AM phantoms,

assessing their suitability for use as axon-mimetic dMRI phantoms. We examine the effects of FDM printing parameters on dMRI acquired in the phantoms, and assess the reproducibility and stability over time of 3AM phantoms' dMRI characteristics.

2.2 Materials and methods

2.2.1 Phantom preparation

An open protocol for producing 3AM phantoms has been developed and released as part of an Open Science Framework project (available in the Supplementary Materials and hosted at osf.io/zrsp6). Required materials include an FDM 3D printer, a dual component "porous filament" material, a vacuum chamber, and a set of watertight containers. The protocol was used to produce all phantoms for this study.

All phantoms were designed using the open-source Ultimaker Cura software, and were printed with an Ultimaker 3 Extended 3D printer (Ultimaker, Geldermalsen, The Netherlands) loaded with GEL-LAY filament. Unless otherwise noted, phantoms were printed with printing parameters recommended by the material vendor (Table 2.1), and the same pattern of parallel lines of material in each layer.

After printing, phantoms to undergo dMRI scanning were immersed in 1L of room temperature water (about 23 °C) for 168 hours, then 20 mL of surfactant was added to decrease surface tension and allow the water to more easily enter the pores. The container was placed in a vacuum chamber at 1 bar for 48 hours to remove air bubbles. Finally, the phantoms were stacked in a test tube with distilled water for imaging (Figure 2.1b-d).

2.2.2 Microscopy

Three block-shaped 3AM phantoms with dimensions 25 mm × 15 mm × 35 mm were printed with vendor-recommended printing parameters. The blocks were immersed in water for 18

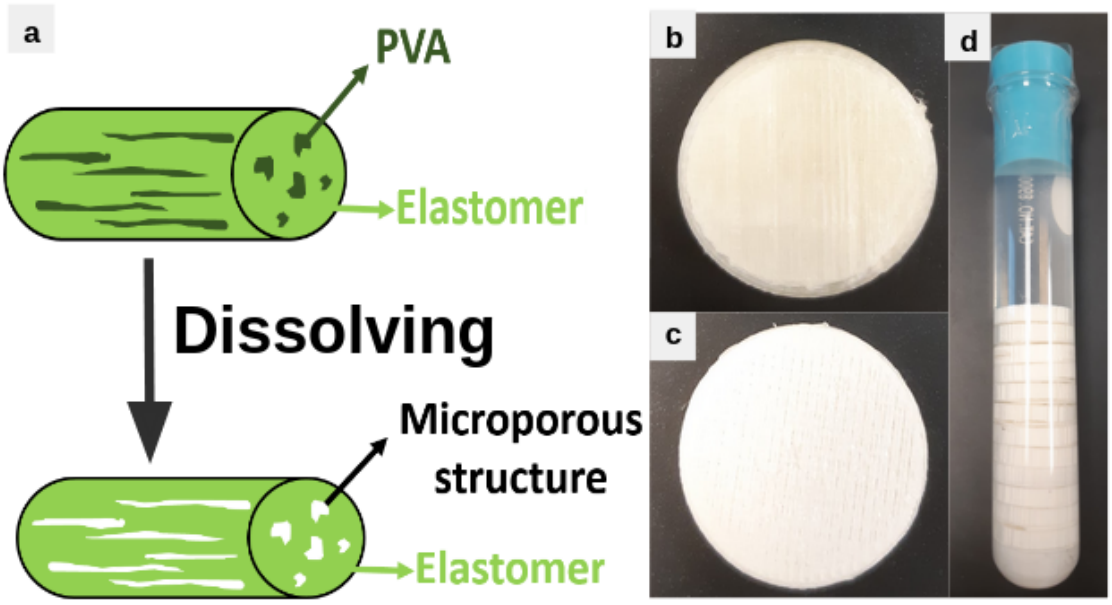

Figure 2.1: Schematic and photographs of 3AM phantoms. (a) PVA dissolves away when placed in water leaving microporous structure. (b) 3AM phantom before dissolving. (c) 3AM phantom after dissolving. (d) Dissolved 3AM phantoms stacked in a test tube with water that are ready for imaging.

hours to soften by allowing a small portion of the PVA to dissolve. Afterwards, the blocks were sliced into 50 µm slices using a Shandon Finesse ME+ microtome (ThermoScientific). The slices were immersed in deionized water for 3 hours to allow the remaining PVA to fully dissolve. They were then immersed in diluted Rhodamine Beta (Rhodamine B) and placed in a vacuum chamber at 1 bar for 20 minutes to infuse the dye into the slices and eliminate air bubbles. The slices were then mounted on positive microscope slides.

Confocal microscopy was performed to obtain high resolution images using a Leica SP5 laser system microscope with a 40X oil-immersion objective lens. Z-stacks of phantom slices were acquired using 1 µm step size for axial ranges from 5 µm to 17 µm. To qualitatively visualize the pores in each sample, every z-stack was either averaged across all slices to produce a 2D image or rendered into 3D volumes using Leica Las X.

Using MATLAB's image processing toolbox, an averaged z-stack confocal microscopy image was converted to grayscale, then an adaptive thresholding technique [43] was used to

compute an initial segmentation of the image. The initial segmentation was opened with a disc-shaped structuring element of radius 1 pixel to eliminate pixels spuriously identified as containing material. The resulting segmentation was then morphologically closed using a disc-shaped structuring element of radius 8 pixels to eliminate small regions spuriously identified as pores. Finally, the equivalent radius of each region identified as a pore was calculated.

2.2.3 Synchrotron phase contrast micro-CT

A cylindrical phantom with a diameter of 5 mm and height of 4.5 mm was 3D printed, immersed in water for two days, and allowed to dry. A propagation-based phase-contrast micro-computed tomography (micro-CT) scan was then performed in air at the Biomedical Imaging and Therapy beamline (05ID-2) at the Canadian Light Source Inc. (Saskatoon, Canada), using an energy of 30 keV, 3000 projections over 180°, 150 ms exposure time and 700 ms time per projection, total scan time of 1 hour, FOV=4096 × 4096 × 3456 μm^3 (L × W × H), and an effective isotropic pixel size of 1.65 μm.

2.2.4 MRI scanning and model fitting

Phantoms to undergo dMRI scanning were all scanned with the same parameters. Diffusion MRI was implemented with a 9.4 T Bruker small animal scanner using a single-shot echo planar imaging sequence with: 120, 60 and 20 directions at b=2000, 1000, and 0 s/mm^2, respectively, TE/TR=37/2500 ms, FOV=200×200 mm^2, 0.7 mm isotropic in-plane resolution, and one 3 mm axial slice per phantom.

For every resulting set of diffusion-weighted images, DiPy [44] was used to compute diffusion kurtosis imaging (DKI) metrics at each voxel with a weighted least squares technique.

A T1-mapping rapid acquisition relaxation enhancement (RARE) scan and a T2-mapping multi-slice-multi-echo (MSME) scan were performed on a set of eight phantoms with different 3D print parameters (Section 2.6). Both scans were implemented with a 9.4 T Bruker small animal scanner, FOV=40×40 mm^2, 0.3125 mm isotropic in-plane resolution, and one 3 mm

axial slice per phantom. The T2 mapping scan was performed with 16 echoes having TE ranging from 6.5 to 104 ms and TR=2000 ms. The T1 mapping scan was performed with TE = 5.7 ms, TRs of 500, 1000, 1500, 2000, and 3000 ms, and ETL = 2. To assess typical T1 and T2 values in 3AM phantoms, the mean and standard deviation T1 and T2 were calculated in the phantom produced with the nominal print parameters recommended by the manufacturer.

2.2.5 Phantoms for assessing the reproducibility of dMRI metrics

Four identical cylindrical 3AM phantoms were prepared with nominal printing parameters following the procedure outlined in Section 2.1. The phantoms were scanned with four axial slices and a scan time of 8.5 min, and DKI was fit to the scan data, all according to the imaging protocol outlined in Section 2.4. The coefficient of variation across all voxels in the phantoms was calculated for each DKI metric to assess the consistency of each metric across phantoms produced under identical conditions.

2.2.6 Phantoms for assessing stability over time and the effect of print parameters on dMRI

Eight cylindrical 3AM phantoms were produced according to the 3AM phantom protocol outlined in section 2.1, each with a width of 22 mm and height of 4.4 mm, composed of 44 layers of parallel lines.

Four FDM print parameters were altered across different phantoms to test their effects on the 3AM phantom's microstructure. The four altered parameters include the temperature at which the phantoms are printed, the speed of printhead travel during the 3D print, the thickness of each layer printed in the phantom, and the infill density, which refers to the proportion of each layer taken up by material, and is altered by changing the distance between adjacent lines of material within each layer. One phantom was printed with the nominal print parameters recommended by the substrate manufacturer, and for each parameter, one phantom was printed

with that parameter lower than nominal, and one phantom with that parameter higher than nominal (where applicable), as summarized in Table 2.1.

The eight phantoms were scanned with four axial slices and a scan time of 8.5 min per each of two dMRI scans to cover the test tube and DKI was fit to the data, all according to the protocol outlined in Section 2.5. The variation in each DKI metric was then assessed across the phantoms with each difference in print parameter.

To investigate the phantoms' stability over longer time periods, identical dMRI scans and model fitting procedures were performed 25 and 76 days later, and the variations in each DKI metric in the phantom produced with nominal parameters across time was assessed.

Printing parameter	Low setting	Nominal setting	High setting
Printing temperature (°C)	215	225	235
Printing speed (mm/s)	20	30	50
Layer thickness (mm)	0.06	0.1	0.14
Infill density (%)	75	100	-

Table 2.1: The parameters used to print the phantoms

2.3 Results

2.3.1 Microscopy

Confocal microscopy images revealed two types of pores present in the phantoms: larger pores (70 μm to 150 μm in diameter) that are believed to have been created by material tearing during the microscopy preparation process and gaps being left between lines of material (Figure 2.2), and smaller pores (1 μm to 30 μm in diameter) created by the dissolving of PVA fibres (Figure 2.3). The images also clearly showed the larger-scale arrangement of each line of material deposited during the 3D printed process.

Segmentation of individual pores showed that there was a peak in the distribution of cross-sectional diameters at about 4 μm to 8 μm, with the distribution having a mean of 20 μm, a

median of 13 µm, and a standard deviation of 20 µm (Figure 2.3).

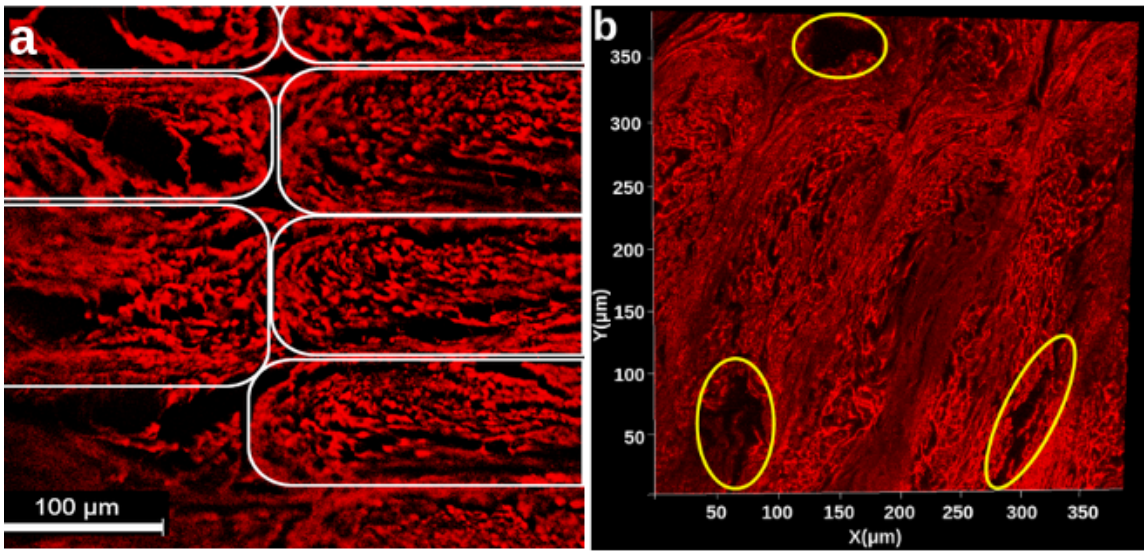

Figure 2.2: Microscopy images of 3AM phantoms. (a) Confocal microscopy z-stack image of a stained cross sectional phantom sample, averaged across slices. Elastomeric matrix (red) and pores (black) are visible. The white outline indicates individual lines of material. (b) 2D projection of a 3D microscopy volume acquired with confocal microscopy. Regions shown in red are the matrix of the 3AM phantom that is composed of elastomer while the black regions are pores. Outlined in yellow are larger pores caused by the printing pattern of the phantom. In both a and b, the image plane is perpendicular to the long axis of the pores.

2.3.2 Micro-CT

The propagation-based phase-contrast micro-CT image showed anisotropic pores that run parallel to the primary travel direction of the 3D print head (Figure 2.4), supporting the findings of the confocal microscopy. These pores had typical diameters on the order of ten microns and typical lengths in the hundreds of microns.

2.3.3 Nominal phantom characteristics and reproducibility

The mean T1 and T2 measured in a phantom printed with nominal printing parameters were 3960 ± 425 ms and 119 ± 21 ms, respectively.

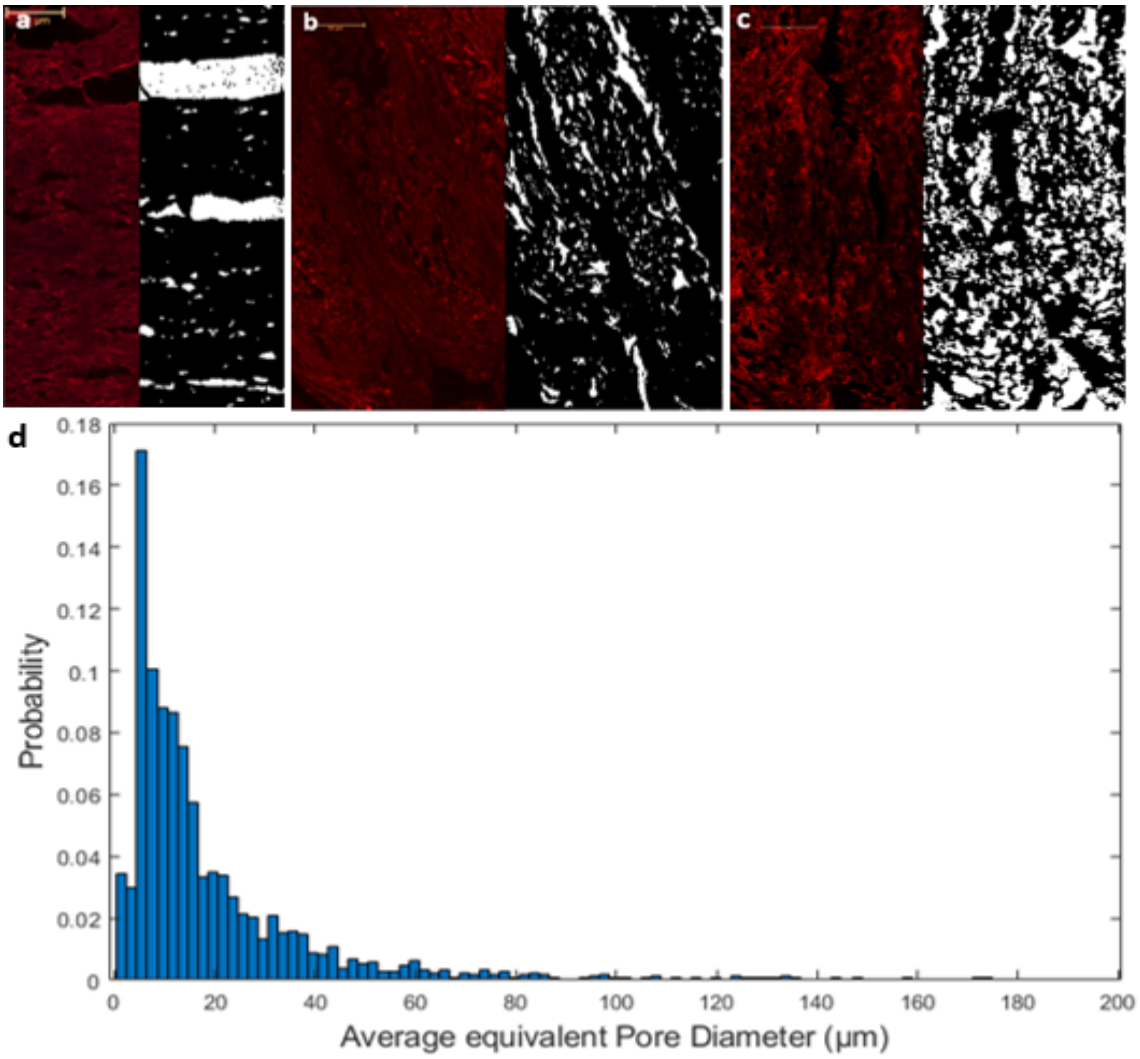

Figure 2.3: Pore segmentation results. (a-c) Confocal microscopy image before (left) and after (right) performing pore segmentation. (d) normalized histogram of equivalent diameter of pores obtained from segmentations in a-c and their frequencies (Total N = 1912).

The mean dMRI characteristics across all voxels of the 4 nominal phantoms are summarized in Table 2.2. The axial diffusivity (AD) is close to the diffusivity of pure water at room temperature ($0.0022\,\mathrm{mm}^2/\mathrm{s}$), and the radial diffusivity (RD) is about half the AD. The axial kurtosis (AK) is close to zero, and the lack of kurtosis in the axial direction is supported by a near-linear relationship between $\ln(S)$ and b from acquisitions with diffusion encoding direction close to the axial direction (Figure 2.5).

The coefficient of variation (%) for each DKI metric across 4 identical nominal phantoms

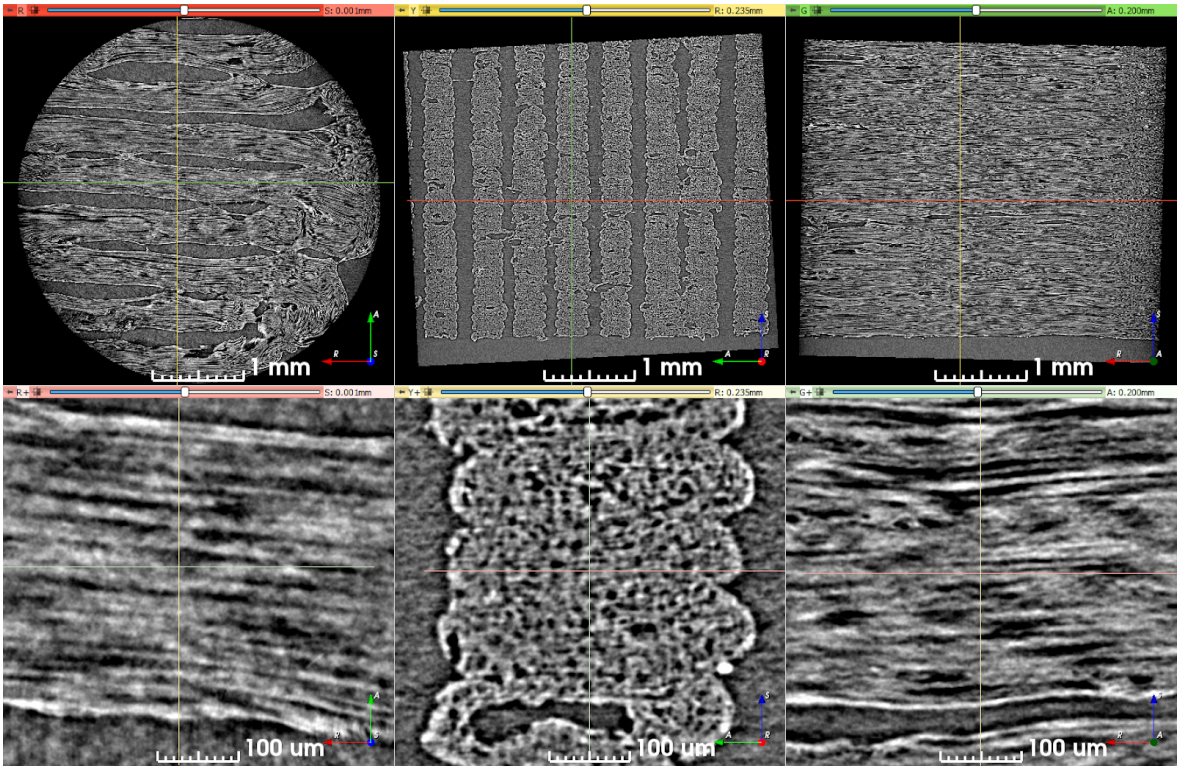

Figure 2.4: Synchrotron micro-CT scan data at two zoom levels, transformed to align lines of material with the viewing planes. Upper row: View of the entire scan ROI. Lower row: Detailed view of a short length of five stacked lines of material. The direction of print-head motion was left-right in the left- and right-most columns, and perpendicular to the image in the center column.

was calculated as a measure of repeatability. The highest coefficient of variation reported was 13.2% for RD, and the rest were lower than 10.5%.

2.3.4 Metric variation with print parameters

Changes in the mean value of each metric with every print parameter were small for every print parameter except infill density (Figure 2.6). Excluding infill density, the difference from the nominal case was less than 16% for all metrics except AK, which had very high percent differences in some cases due to mean values close to zero. An increase in infill density of the phantom resulted in an increase in fractional anisotropy and a decrease in radial diffusivity.

Metric	Mean value	Standard deviation	Coefficient of variation (%)
AD (10^{-3} mm^2/s)	2.13	0.05	3.19
RD (10^{-3} mm^2/s)	1.01	0.08	13.20
MD (10^{-3} mm^2/s)	1.38	0.07	8.78
FA	0.46	0.03	5.24
AK	0.07	0.01	10.10
RK	1.13	0.07	6.31
MK	0.52	0.02	1.86

Table 2.2: Mean dMRI metrics from four phantoms and their coefficient of variation.

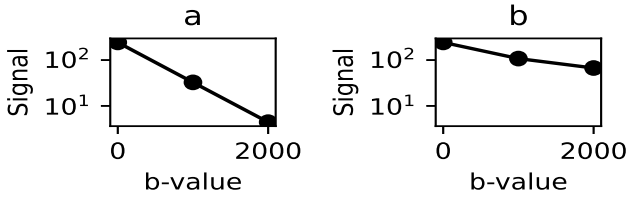

Figure 2.5: Expected signal vs. b-value from the DKI fit in: (a) the axial direction, and (b) the radial directions.

2.3.5 Metric stability over time

Over the 76 days of study, only small differences in mean value were observed for all metrics ($< 7\%$, except for AK due to some very small values of AK), as seen in Figure 2.7.

2.4 Discussion

2.4.1 Phantom vs. human microstructural fibre geometry

Microscopy images and synchrotron micro-CT images both indicate the presence of densely packed fibrous pores within a 3D printed composite material containing PVA within an elastomeric matrix. With typical diameters from 1.5 µm to 8 µm (Figure 2.3), these fibrous pores are larger than typical axons [17]. However, the fibres are still narrow enough to modulate the diffusion signal at diffusion times typical for dMRI studies, so they can approximately mimic

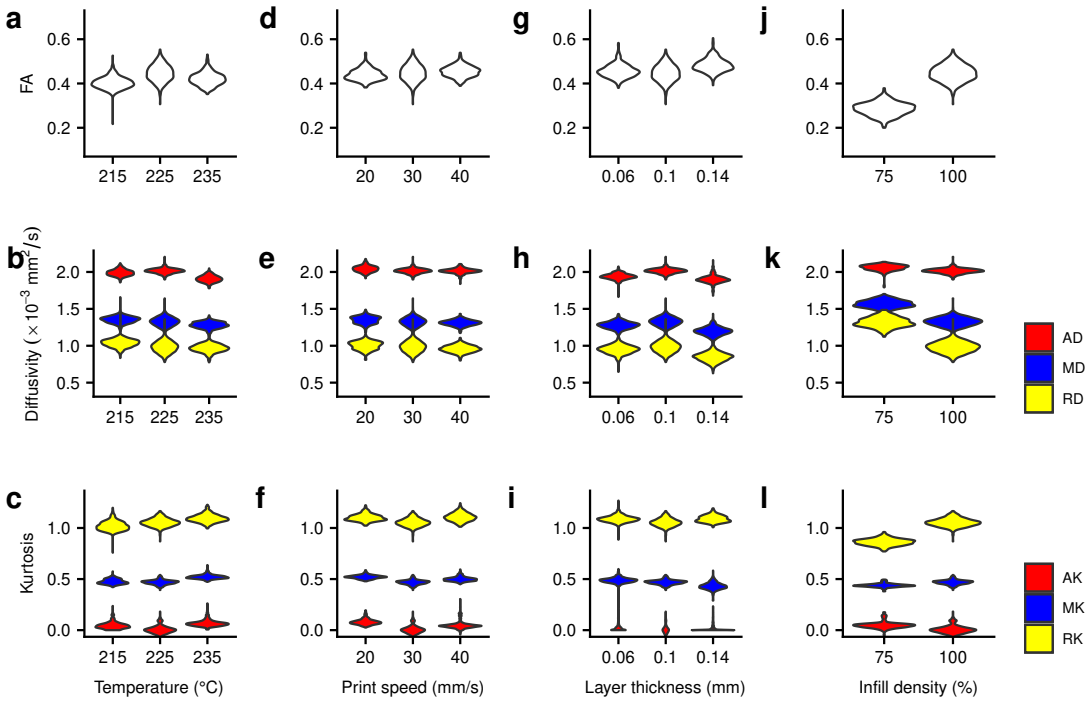

Figure 2.6: FA, diffusivities, and kurtosis of phantoms printed with different printing parameters. (a-c) DKI metrics vs. printing temperature. (d-f) DKI metrics vs. printing speed. (g-i) DKI metrics vs. layer thickness. (j-l) DKI metrics vs. infill density.

the anisotropic diffusion characteristics of axonal bundles. Notably, there may be smaller pores present that the confocal microscopy was unable to resolve which may have skewed the histogram to larger diameters. Future work could use electron microscopy to resolve such smaller pores. Nevertheless, the protocol introduced by this study produces long, straight pores that have a limited effect on diffusion along their path.

2.4.2 Phantom vs. human diffusion characteristics

The observed DKI metrics correspond well to those seen in real white matter but have some notable differences. The phantoms were scanned at room temperature, which has a lower diffusivity of free water (about 0.0022 mm^2/s) than human body temperature (about 0.003 mm^2/s) [45]. This difference in the diffusivity of free water means that the diffusivity DKI metrics have a higher maximum possible value in vivo, which should be accounted for when analyzing those

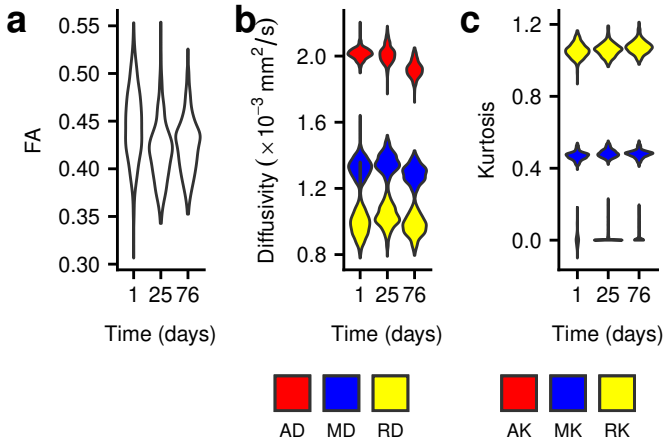

Figure 2.7: DKI metric stability in a nominal phantom over 76 days. (a) FA. (b) Diffusivities. (c) Kurtosis.

metrics.

AD in the phantoms was close to the diffusivity of free water at room temperature, while coherently organized white matter in the brain typically has AD of about 0.001 mm^2/s, roughly a third of the diffusivity of free water at body temperature [46]. This discrepancy indicates that the uniform fibre orientation and homogeneous microstructure of the phantoms results in a simpler axial diffusion environment than that observed in the brain. AK in the phantoms was close to zero, while practically all white matter regions in the brain have non-zero AK. This finding further supports the conclusion that there is an anatomically unrealistic homogeneity in the phantoms' microstructure; real tissue is more heterogeneous and structurally complex than the 3AM phantoms.

RD in the 3AM phantoms was much lower than the diffusivity of free water at room temperature, indicating that diffusion is hindered and/or restricted perpendicular to the axis of the pores. The mean RK in the nominal 3AM phantom is non-zero but lower than typical values in orientationally coherent white matter tracts [47]. This indicates that the fibrous pores of the 3AM phantom restrict diffusion but do not recreate the structural heterogeneity of real white matter.

MD in the 3AM phantoms was about 63% of the diffusivity of free water at room tempera-

ture, while MD in real white matter is typically less than 33% of the diffusivity of water at body temperature. Partially due to the near-total lack of restriction or hindering of diffusion in the axial direction, there is less restriction/hindering of diffusion overall in 3AM phantoms than in white matter. MK in the 3AM phantoms was about half the typical values in human white matter [47], further indicating that 3AM phantoms have less heterogeneous microstructure than real axonal tracts.

The FA is within the range of typical values observed in the human white matter [46], but lower than some of those observed in the most coherent regions like the corpus callosum, which can reach above 0.6 [46]. The micro-CT images show gaps between adjacent lines of material even at 100% infill density, which leads to a non-negligible free water compartment within the phantoms. This free water compartment reduces the overall FA due to partial voluming, which suggests that a higher FA may be achievable with an altered 3D printing process. This free-water compartment likely also contributes to the relatively low kurtosis values and the diffusivities being relatively close to the free water value.

2.4.3 Phantom reproducibility and stability

Infill density was the only print parameter that had a large effect on any of the DKI metrics, with its greatest effect on FA, RD, and RK. The likely explanation for this effect is that a lower infill density replaces the elastomeric matrix with free water, increasing the effect of partial voluming between the two components.

The small effect of the other 3D print parameters on the observed DKI metrics suggests that minor variations in print parameters across different 3D printers should not greatly affect the characteristics of the phantoms they print. However, this also means that it is likely not possible to change print parameters to tune a phantom's diffusion characteristics. That said, it may be possible to tailor diffusion characteristics using different porous filament materials. The low coefficient of variation across identical phantoms supports the conclusion that the 3AM phantom production protocol is repeatable, at least across multiple prints on a single

printer with the same material.

The stability analysis showed only small changes over the time period of 2.5 months. This demonstrated stability of the phantom microstructure over a relatively long time period suggests that one prepared phantom sample can at least be transported to multiple sites in multi-centre studies without concern for parameter changes between scans.

2.4.4 Method advantages

The phantoms we have introduced are produced with FDM 3D printing, a widely accessible and inexpensive production technique. A single spool of printing material (about $50 USD) can be used to produce hundreds of phantoms. The development of this technique lowers the barrier to entry for researchers to conduct phantom studies for validation of certain dMRI models of white matter. Such studies bridge the gap between simulations and studies using fixed tissue, serving as a useful option for the dMRI modeling community.

The three analyses performed for this study show the existence of axon-mimetic fibrous pores in 3AM phantoms that modulate dMRI signal to approximate white matter anatomy. By analyzing the microstructure of the phantoms with both confocal microscopy and phase contrast micro-CT, we have confirmed that the fibrous pores in our phantoms are of an appropriate size and shape to mimic axonal fibres. These findings are supported by the observation of non-zero FA and RK. Furthermore, the quantitative T1 and T2 scans indicate that the phantoms do not shorten relaxation times enough to significantly reduce SNR in dMRI scans, and they can be reduced via doping (e.g., copper II sulphate) to better agree with values found in tissue.

FDM offers the flexibility to alter the print-head direction between layers, which may enable the exploration of crossing fibre effects and their associated models. In our preliminary investigations, FA reductions are observed with increasing fibre crossing angle. Future work will investigate optimal phantom design for validation of crossing fibre models.

2.5 Conclusion

In this study we introduce 3AM phantoms, a novel class of dMRI phantoms that are customizable, affordable, and straight-forward to produce. 3AM phantoms mimic the microporous structure of axon bundles in white matter, and the utilization of 3D printing likely opens the door for customizability and the production of complex, anatomically accurate phantoms.

Chapter 3

Characterization of fibre geometry's effect on diffusion MRI models

3.1 Introduction

Diffusion MRI (dMRI) is an imaging modality that measures signal that is sensitive to the diffusion of water molecules on a microscopic scale. The dMRI signal in a voxel containing one or more axonal fibres is determined by both the microstructure and the orientation of the fibres. Diffusion MRI models of white matter characterize microstructure and orientation with varying levels of sensitivity and specificity. Discriminating between signal variation caused by microstructural changes and signal variation caused by orientational changes is difficult, and dMRI models are known to characterize microstructure less precisely in the presence of orientation dispersion, where fibre segments with different orientations within a single voxel cause partial volume errors [48]. These complex fibre configurations are widespread in the human brain [49], so the ideal dMRI model of white matter would characterize both microstructure and orientation accurately and robustly.

To validate dMRI models of white matter, it would be useful to quantify the effect of orientation dispersion on those models' estimated parameters. However, it is difficult to perform

that quantification because there is no widely accepted complementary modality to provide a ground truth of axonal orientation in vivo. Instead, numerical or physical phantoms can provide that ground truth [16]. Numerical phantoms allow fine-grained control of the sample, but lack the fidelity of real scan data. Physical phantoms offer real scan data with a ground truth. However, existing physical fibre-containing phantoms tend to be expensive and time-consuming to prepare, with limited orientational complexity.

Fused deposition modeling (FDM) 3D printing offers a promising technology for producing dMRI phantoms, if an appropriate material is used. GEL-LAY (LAY Filaments, Cologne, Germany) is an FDM filament composed of an elastomeric matrix containing pockets of polyvinyl alcohol (PVA). When 3D printed, the pockets of PVA form fibres with a long axis oriented along the direction of motion of the print head. When immersed in water, the PVA dissolves, leaving microscopic fibrous pores that can mimic the diffusion characteristics of axonal fibres, with known primary directions of diffusion. By 3D printing an object with a known pattern of fibres, a phantom can be produced that is useful for examining the behaviour of dMRI models of white matter in the presence of specific fibre configurations [50]. These 3D printed axon-mimetic (3AM) phantoms are inexpensive and effective, but have not yet been used to produce a phantom with complexity beyond crossing fibres.

Here, we introduce a custom software extension that enables 3D printers to produce bending, kissing, and fanning patterns. We then use phantoms 3D printed with this extension to characterize the effect of those complex geometries on dMRI models.

3.2 Methods

A custom extension to the Ultimaker Cura 3D printer software was developed to allow within-layer fibre configurations composed of concentric arcs, in addition to the patterns composed of parallel lines available by default.

We used the Cura extension to prepare and 3D print five phantoms (Figure 3.1). The phan-

toms were cylindrical, with a radius of 11 mm and height of 4.5 mm. Each phantom had a different pattern of within-layer fibre configurations, where each print layer is 0.1 mm thick. These phantoms are described in Table 3.1.

Label	Phantom description
Bending	Every layer has the same pattern of concentric arcs, with a centre 10 mm from the phantom's centre.
Straight	Every layer has an identical pattern of parallel lines.
Kissing	Layers alternate between straight lines and concentric arcs with a centre 6.5 mm from the phantom's centre.
Fanning	Layers alternate between two patterns of concentric arcs with centres 10 mm apart.
Crossing	Layers alternate between two patterns of parallel lines with perpendicular directions.

Table 3.1: The phantom fibre configurations.

The three phantoms with spatially heterogeneous fibre configurations (i.e. the bending, fanning, and kissing phantoms) were printed with a triangular hole to serve as a fiducial.

We performed a dMRI scan of the phantoms using a single-shot echo planar imaging sequence with: 20, 50, and 120 volumes acquired at b = 0, 1000, and 2000 s/mm^2 respectively, TE/TR=37/2500 ms, FOV=200×200 mm^2, 0.7 mm isotropic in-plane resolution, and 6 axial slices with a thickness of 3 mm each (one slice per phantom and one slice in water).

For the fanning, bending, and crossing phantoms, we localized the phantom's centroid and fiducial in the mean Diffusion Weighted Image (DWI), and used those points to produce ground truth images of crossing angle or radius of curvature, as appropriate, registered to the captured image space.

DIPY [44] was used to perform weighted ordinary least squares fits of Diffusion Tensor Imaging (DTI) [8], using only the acquisitions at b = 0 and 1000 s/mm^2; and Diffusion Kurtosis Imaging (DKI) [9, 10] representations to the DWI's. Four parameters were then extracted from the DTI fit: axial diffusivity (AD), which quantifies the estimated diffusivity along a central axis; radial diffusivity (RD), which quantifies the diffusivity in the directions perpendicular

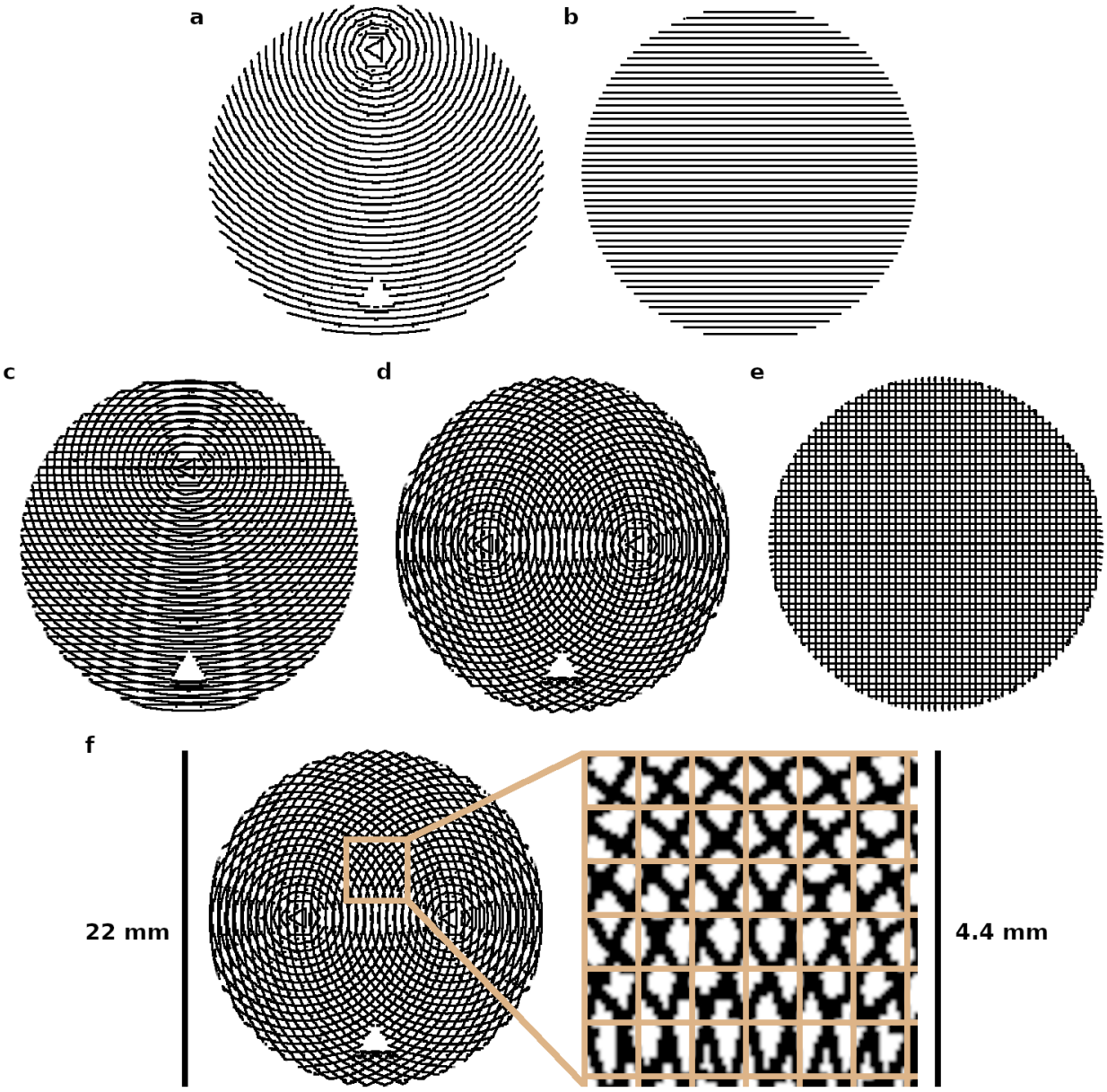

Figure 3.1: The five phantom patterns, with alternating layers superimposed on one another, and a demonstration of the phantoms' scale. (a) Bending. (b) Straight. (c) Kissing. (d) Fanning. (e) Crossing. (f) The fanning phantom with a magnified view including the 0.7 mm isotropic in-plane voxel size superimposed.

to that central axis; mean diffusivity (MD), which quantifies the mean diffusivity across all directions; and fractional anisotropy (FA), which quantifies the degree to which diffusion in a voxel is anisotropic. The same four diffusivity-based metrics are extracted from the DKI,

in addition to three kurtosis metrics, which capture the degree to which diffusion in a voxel deviates from Gaussianity: axial kurtosis (AK), radial kurtosis (RK), and mean kurtosis (MK).

The Microstructure Diffusion Toolbox (MDT) [7] was used to perform Powell conjugate-direction optimized fits of ball and stick [11], NODDI [12], and Bingham-NODDI [13] models to the DWI. All models' assumed diffusivities were fixed at $2.2\,\mathrm{mm}^2/\mathrm{s}$, the diffusivity of pure water at room temperature, based on the DTI diffusivity metrics observed in a straight phantom [50]. The single parameter extracted from the ball and stick model is the relative volume fraction between the ball compartment and the stick compartment. NODDI and Bingham-NODDI both produce volume fractions of intra-neurite, extra-neurite, and CSF compartments. NODDI also produces the orientation dispersion index (ODI), which quantifies from 0 to 1 the dispersion of the Watson distribution that governs the intra- and extra-neurite compartment. Bingham-NODDI splits ODI into a primary ODI ($\mathrm{ODI_P}$), and a secondary ODI ($\mathrm{ODI_S}$), quantifying the anisotropic dispersion described by the Bingham distribution.

For each dMRI model parameter, we fit three quadratic regression models: the parameter vs. radius of curvature in the bending phantom, and the parameter vs. crossing angle in the kissing and fanning phantoms. The R^2 was used to quantify how much dMRI model variance was accounted for by each regression model.

3.3 Results

We fit each of DTI, DKI, Ball and Stick, NODDI, and Bingham-NODDI to scan data from five phantoms, each of which represented one of fanning, kissing, bending, crossing, or straight fibres. The 3D printed phantoms represent a spectrum of fibre geometry complexities, from straight fibres at simplest, to fanning fibres at most complex. For the three phantoms with varying degrees of orientation dispersion, we registered a ground truth of either radius of curvature or crossing angle to the scan data. Then, for each dMRI model parameter and orientation dispersion metric, we performed a quadratic regression with the model parameter as the depen-

dent variable and the orientation dispersion metric as the independent variable. The results of this procedure are summarized in Figure 3.2.

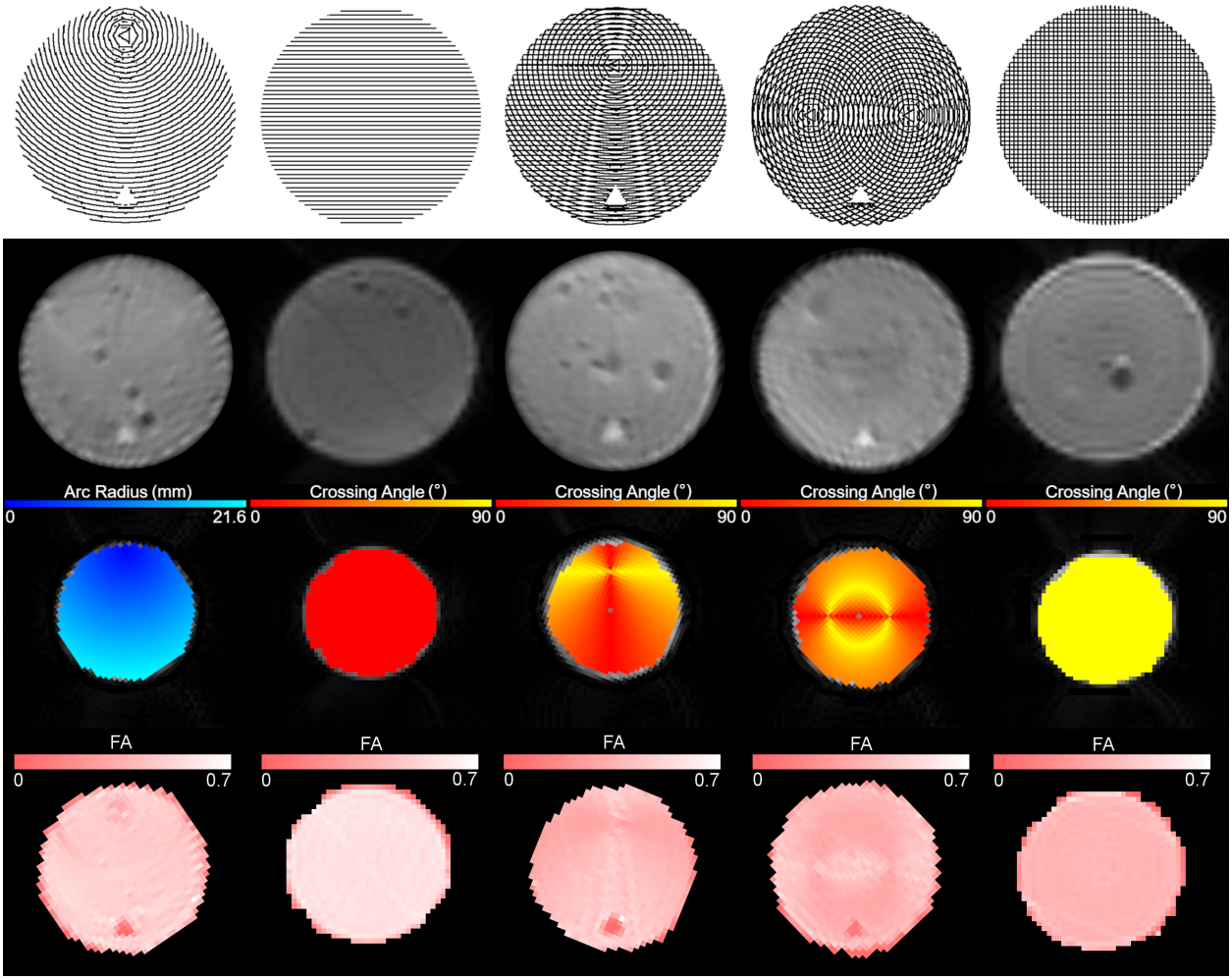

Figure 3.2: A summary of the results. From left to right, the columns correspond to the bending, straight, kissing, fanning, and crossing phantoms. The top row shows the schematic of each phantom, the second row shows an image of each phantom without diffusion weighting, the third row shows the ground truth description registered to image space, and the fourth row shows the DTI-derived FA map of each phantom as an example.

3.3.1 DTI

Figure 3.3 plots the DTI metrics in each phantom against the orientation dispersion in that phantom. The DTI metrics without dispersion in the straight phantom are consistent, and

describe a very anisotropic diffusion signal with axial diffusivity of about 2.2 mm^2/s, and RD roughly a third of that, leading to an FA of about 0.65. The DTI metrics in the straight phantom have less variance than the same metrics in the other phantoms.

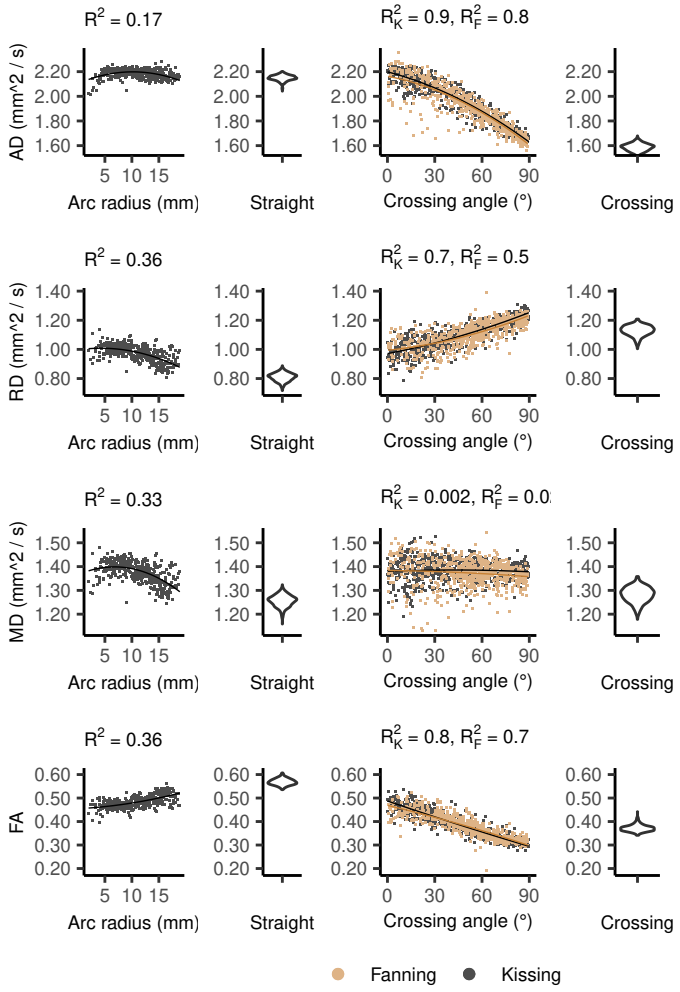

Figure 3.3: DTI metrics vs. orientation dispersion metrics in each of the four phantoms. Each row depicts the relationship between one metric and orientation dispersion, and each column depicts the data from one or two phantoms. From left to right, those phantoms are: bending, straight, fanning and kissing, and crossing.

Arc radius in the bending phantom accounted for some of the variance in all four DTI metrics. AD appears to increase with arc radius before plateauing at an arc radius of about 5 mm, after which the distribution of AD matches that found in the straight phantom. RD decreases as arc radius increases. However, RD's distribution at the highest arc radii in the

bending phantom remains higher than the distribution in the straight phantom. MD increases with arc radius until about 5 mm, at which point it begins to decrease. Similarly, FA shows little variation at lower arc radii but begins to increase with arc radius at about 5 mm.

The fanning and kissing phantoms show stronger relationships between the two primary DTI diffusivity metrics and crossing angle. AD decreases with crossing angle to about 70% of its value at zero degrees. At low crossing angles RD is higher than the values seen in the straight phantom. RD increases further with crossing angle to about 125% of its value at zero degrees. Crossing angle explains little of the variance in MD. Conversely, crossing angle explains most of the variance in FA.

In the crossing phantom, the AD distribution largely agrees with the AD at high crossing angles in the fanning and kissing phantoms. The RD, however, is lower in the crossing phantom than at high crossing angles.

3.3.2 DKI

The DKI diffusivity metrics show similar patterns to those observed in DTI, but with less pronounced relationships between diffusivity metrics and orientation dispersion metrics.

In the straight phantom there is little axial kurtosis (AK) and a median radial kurtosis (RK) of about 1.15 (Figure 3.4). Those metrics combine to produce a mean kurtosis of about 0.55.

Arc radius explains little of the variance in AK in the bending phantom, and there is good agreement between the AK distributions in the bending and straight phantoms. The bending phantom demonstrates an increase in RK with increasing arc radius. The highest RK values in the bending phantom are lower than those seen in the straight phantom. Arc radius also explains little of MK's variance in the bending phantom, but the straight phantom has a higher distribution of MK than the bending phantom.

The fanning and kissing phantoms demonstrate relationships between kurtosis and crossing angle. AK's distribution at low crossing angles agrees with the distribution in the straight phantom, and barely changes below 45 degrees, but does increase with crossing angle beyond

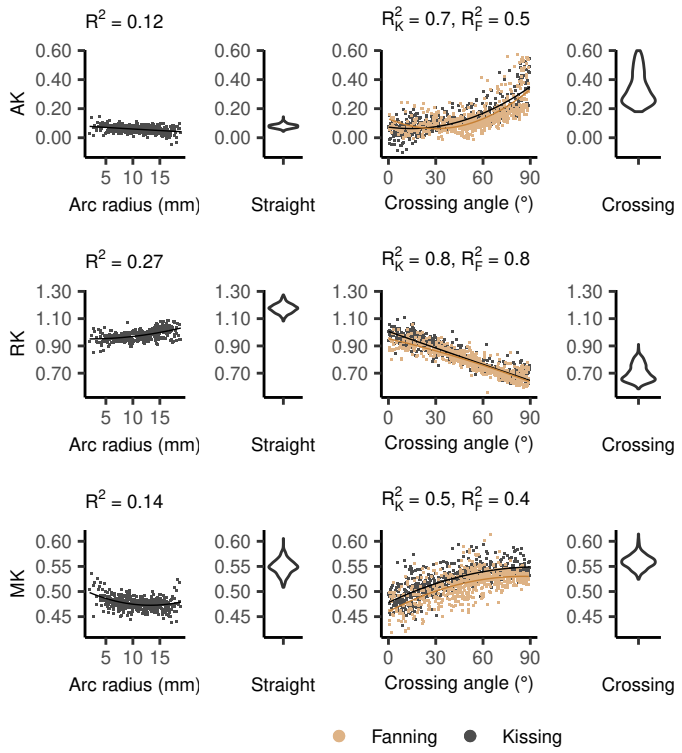

Figure 3.4: DKI kurtosis metrics vs. orientation dispersion metrics in each of the four phantoms. Each row depicts the relationship between one metric and orientation dispersion, and each column depicts the data from one or two phantoms. From left to right, those phantoms are: bending, straight, fanning and kissing, and crossing.

that point. In addition, AK's unexplained variance increases with crossing angle beyond 45 degrees. RK decreases almost linearly with increasing crossing angle from a distribution lower than that of the straight phantom to a distribution that agrees with the crossing phantom. At low crossing angles, MK's distribution is lower than that of the straight phantom, but it plateaus at about 60 degrees with a distribution that agrees with the crossing phantom.

In the crossing phantom, all three metrics agree with the distribution at higher crossing angles in the fanning and kissing phantoms. Compared to the straight phantom, the crossing phantom shows a difference in median AK and RK, and more variance in those metrics. However, the MK distribution is very similar between the two phantoms.

3.3.3 Ball and Stick

Figure 3.5 shows the ball and stick volume fractions in each phantom. The straight phantom is assigned a stick volume fraction of about 0.32, roughly half the ball volume fraction.

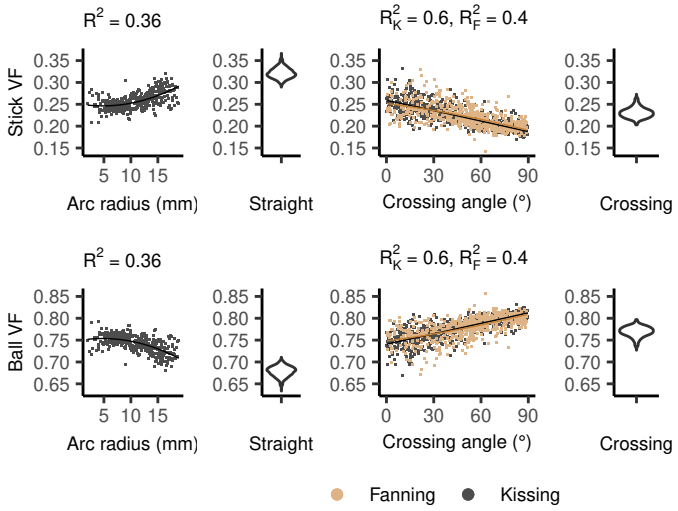

Figure 3.5: Ball and stick volume fractions vs. orientation dispersion metrics in each of the four phantoms. Each row depicts the relationship between one metric and orientation dispersion, and each column depicts the data from one or two phantoms. From left to right, those phantoms are: bending, straight, fanning and kissing, and crossing.

In the bending phantom, the stick volume fraction increases from a mean of about 0.25 at low crossing angles to a mean close to 0.3 at higher crossing angles. The distribution does not reach the stick volume fraction in the straight phantom.

In the fanning and kissing phantoms, the stick volume fraction decreases from a mean of about 0.25 to a mean of about 0.2. At low crossing angles, the distribution is lower than in the straight phantom, and at high crossing angles, the distribution is lower than in the crossing phantom.

3.3.4 NODDI

Figure 3.6 shows the NODDI parameters for each phantom. In all phantoms, there is a bimodal distribution of volume fraction assigned to the CSF and the extra-neurite compartments.

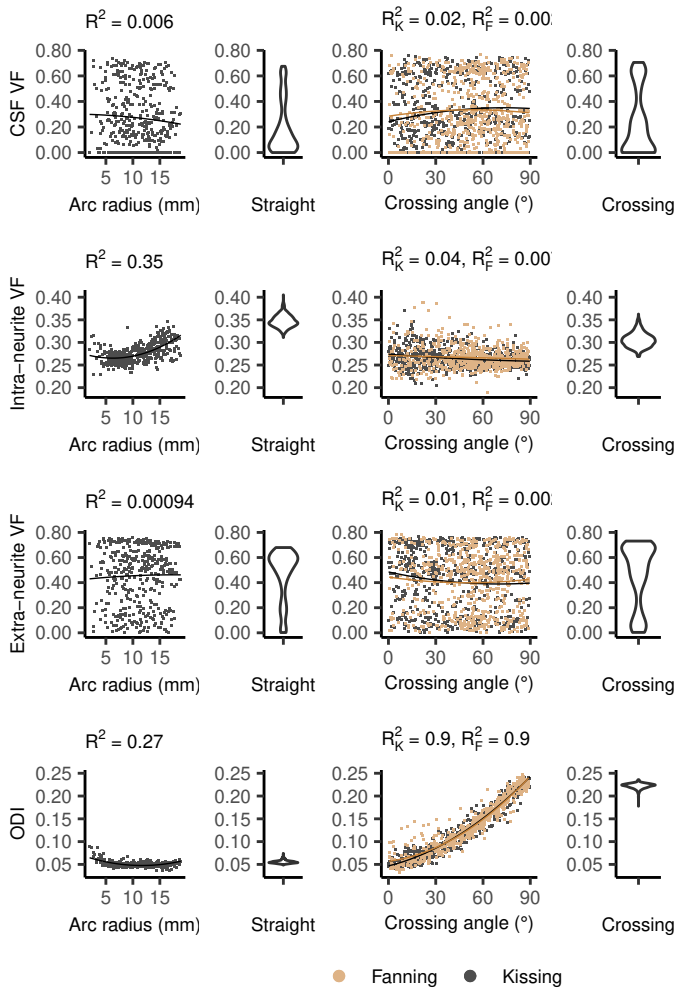

Figure 3.6: NODDI metrics vs. orientation dispersion metrics in each of the four phantoms. Each row depicts the relationship between one metric and orientation dispersion, and each column depicts the data from one or two phantoms. From left to right, those phantoms are: bending, straight, fanning and kissing, and crossing.

In the bending phantom, Intra-neurite volume fraction increases at higher arc radii, but does not reach the distribution seen in the straight phantom. ODI decreases as arc radius increases from about 0 mm to 5 mm, then settles at about 0.4 mm, agreeing with the value in the straight phantom.

In the kissing and fanning phantoms, any variance in compartment volume fraction caused by crossing angle is dominated by variance caused by other factors. ODI, however, has a nearly linear relationship with crossing angle, increasing from about 0.05 at 0 degrees to about 0.24

at 90 degrees, values which agree with the distributions in the straight and crossing phantoms.

3.3.5 Bingham-NODDI

Figure 3.7 plots the Bingham-NODDI parameters in each phantom against the orientation dispersion in that phantom. The secondary orientation dispersion index (ODI_S) is about 0.01 across the sample, so it is not plotted.

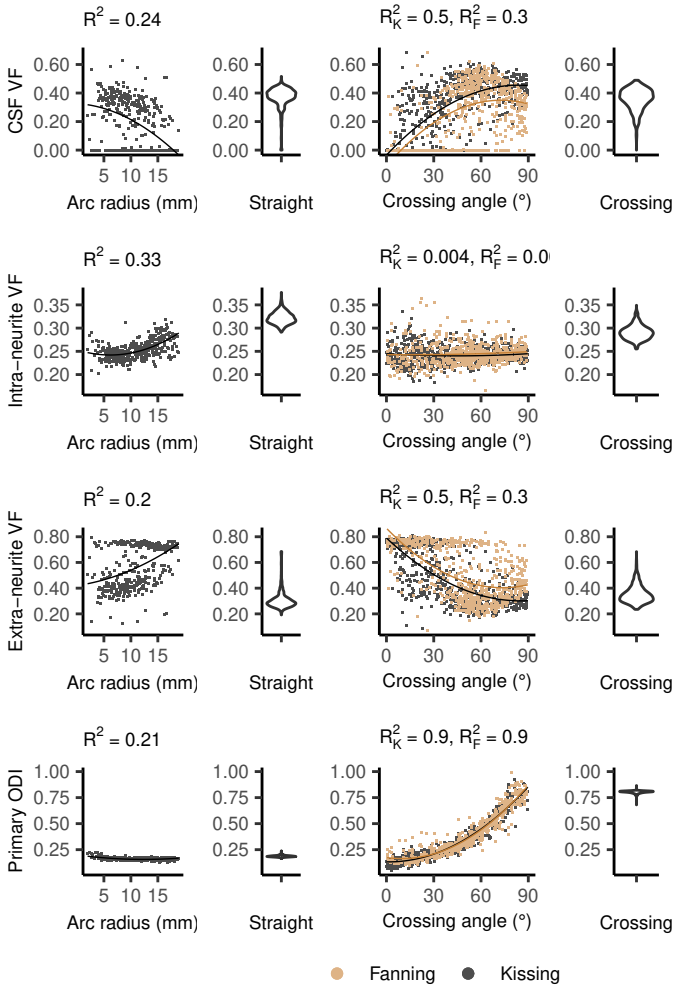

Figure 3.7: Bingham-NODDI metrics vs. orientation dispersion metrics in each of the four phantoms. Each row depicts the relationship between one metric and orientation dispersion, and each column depicts the data from one or two phantoms. From left to right, those phantoms are: bending, straight, fanning and kissing, and crossing.

The intra-neurite compartment is consistently assigned a volume fraction close to 0.25. The

intra-neurite volume fraction appears to increase with higher radii of curvature, but does not appear to be affected by fibre crossing angle.

Like the NODDI fit, the Bingham-NODDI fit also shows a split in the volume fraction assigned to the CSF and extra-neurite compartments: in most voxels, the CSF volume fraction is either zero or close to 0.4. Unlike NODDI, the split appears to be biased by orientation dispersion: at high crossing angles and low radii of curvature, volume fraction appears more likely to be assigned to the CSF compartment.

In the crossing phantom, all metrics agree with the distributions in the kissing and fanning phantoms at high crossing angles. There is a high amount of overlap between the volume fraction distributions of the straight and crossing phantoms. Conversely, there is a large difference in ODI_P between the straight and crossing phantoms.

3.4 Discussion

The results showed how diffusion MRI model parameters respond to fibre curvature and fibre crossings in five 3D printed phantoms. A number of patterns emerge across the five models we investigated. Fibre curvature and crossing angle usually both affect model metrics, with decreasing radius of curvature and increasing fibre crossing angle changing the metric in the same direction (but often by a different amount). We can refer to both changes as an increase in fibre orientation dispersion, as both broaden the number of directions in which water molecules can diffuse within one voxel without encountering a barrier. Both forms of orientation dispersion also contradict the idea of a central axis of diffusion assumed by some models, and this affects the performance of those models in different ways.

In DTI, both forms of orientation dispersion increase RD and decrease AD. In DKI, orientation dispersion increases AK, decreases RK, and increases MK. In the ball and stick model, orientation dispersion increases the ball volume fraction. In NODDI, orientation dispersion increased the ODI. In Bingham-NODDI, orientation dispersion increased CSF volume fraction,

decreased, extra-neurite volume fraction, and increased primary ODI.

3.4.1 DTI

In DTI, increased orientation dispersion of either form increases RD and decreases AD, bringing the two metrics closer together and reducing the FA. Fibre crossings have a stronger effect on these metrics than fibre curvature does, which is consistent with the overall lower levels of fibre dispersion for bending at the arc radii used here compared to crossing fibres. This drop in FA between straight and orthogonally crossing fibres observed in physical phantoms replicates prior simulation findings [48], and shows a linear relationship between crossing angle and FA. MD does not appear to systematically change with fibre crossing angle, which is expected due to the rotational invariance of MD at both the micro- and macroscopic level. MD behaves differently with arc radius, increasing with fibre curvature but having little response to fibre crossings. This behaviour may be due to phantom characteristics at high angles of curvature; for example, there may be larger gaps between 3D-printing lines at lower arc radii, which would explain the slightly increased MD.

3.4.2 DKI

DKI's consideration of non-Gaussian diffusion causes the more subtle changes in diffusivity metrics in DKI than in DTI; kurtosis metrics account for some of the signal variation with increased orientation dispersion. MK increases with both forms of orientation dispersion, which is expected given that mean kurtosis increases with orientation dispersion [51]. The directional kurtosis metrics change more than the MK, which is consistent with the lack of a well-defined dominant eigenvector as orientation dispersion decreases.

3.4.3 Ball and stick

Fibre curvature with a radius as high as 18 mm has an effect on the ball and stick model. Fibre curvature and crossing angle both appear to affect volume fractions in the ball and stick model. The presence of either form of orientation dispersion decreases stick volume fraction. The stick compartment represents one central axis in a voxel along which there is a greater amount of diffusion than in any other direction. In voxels with significant fibre curvature or multiple fibres, a single central axis of diffusion does not exist, so the stick compartment is assigned less volume as a result.

3.4.4 NODDI

The 3AM phantoms in this study essentially have two major compartments: space within the microscopic fibrous pores, which is expected to act like intra-neurite space; and free water between lines of extruded material. NODDI consistently characterizes the intra-neurite space with its intra-neurite compartment, but the unstable ratio of volume fraction assigned to the CSF and extra-neurite compartments suggests that the two compartments describe the free water space roughly equivalently. This apparent similarity between the two compartments is partially explained by the tortuosity model included in NODDI: with intra-neurite volume fractions consistently around 0.3, the cylindrically symmetric diffusion tensors that make up the intra-neurite compartment have a radial diffusivity about 70% of the axial diffusivity, meaning that the tensors are not strongly anisotropic. A phantom with a more structurally complex microstructure including a third compartment may elicit a more consistent response from NODDI. However, NODDI's CSF volume fraction has been also been reported to have low reproducibility in vivo [52].

NODDI's volume fraction metrics have limited sensitivity to the orientation dispersion presented by these phantoms, which suggests that large changes in NODDI's volume fraction metrics indicate changes to the microstructural fibre composition, as intended. NODDI's ODI metric does change reliably with fibre crossing angle, suggesting that it may be a robust indica-

tor of orientation dispersion. However, the planar patterns of orientation dispersion in the 3AM phantoms challenge the Watson distribution: to distribute the intra-neurite compartment's orientation along a plane, it needs to distribute it equally perpendicular to that plane. There is an inherent trade-off between the accuracy of the predicted diffusion pattern in-plane and out-of-plane. This trade-off forced by NODDI's use of the Watson distribution led to the development of Bingham-NODDI. However, the planar pattern of diffusion in 3AM phantoms does limit their ability to test NODDI's response to 3D dispersion, which may occur in the brain.

3.4.5 Bingham-NODDI

While Bingham-NODDI has a similar unstable fit to NODDI, with both the CSF compartment or the extra-neurite compartment describing the free water in the phantoms approximately equally precisely, orientation dispersion does affect the balance between the two cases, unlike NODDI. Regions with less orientation dispersion are more often assigned no volume fraction of CSF.

The high sensitivity of ODI_P to fibre crossing angle demonstrates that the Bingham distribution is able to accommodate the planar patterns of diffusion observed in the 3AM phantoms, which the Watson distribution cannot do. ODI_P spans its entire defined range in the fanning and kissing phantoms, granting this metric high sensitivity to crossing fibres.

3.4.6 Phantom performance

For this study, the 3D printed phantoms provide a ground truth with consistent microstructure but controlled orientation dispersion. The design of the 3D printed phantoms used in this study allowed the effect of fibre curvature to be separated from the effect of crossing fibres. Both are forms of orientation dispersion observed in the brain, and both have distinct effects on dMRI models of white matter. The metrics in NODDI and Bingham-NODDI meant to capture orientation dispersion as a whole showed higher sensitivity to fibre crossings than to fibre curvature.

This work illustrates a physical dMRI phantom that produces a biophysically plausible ground truth for diffusion signal in the presence of complex fibre configurations like fanning and kissing fibres. While analyses similar to those presented here were previously available using simulated data [48], the level of orientational complexity easily achievable with physical phantoms was more limited. The 3D printed phantoms therefore fill a previously empty niche in the spectrum of phantoms available for the validation of dMRI, offering a control over the ground truth greater than that available for ex-vivo tissue and some existing physical phantoms, along with the fidelity associated with performing a physical scan rather than a numerical simulation.

The nature of the 3D printing technique used to produce the phantoms left some artifacts in the phantom. Arcs are printed in short, straight segments, and those segments are long enough to be individually visible in the shorter arcs. In these cases, the printed pattern is a poor approximation of an arc. The layer-by-layer 3D printing procedure also means that the complex geometries are restricted to a single plane. In other words, the diffusion parallel to the axis of the cylindrical phantoms is constant, regardless of the in-plane print pattern. This limits the geometric complexity achievable with the 3D printed phantoms.

There is not a complete model of the diffusion signal from the 3D printed phantoms. While we know in general terms that the material is made up of fibrous pores that restrict diffusion anisotropically, we do not have a precise characterization of the distribution of those pores' radii, or the volume fractions of porous space, free water, and elastomeric matrix. With such a characterization, it would be possible to validate the values of any given dMRI model in addition to the trend with orientation dispersion, as we did in this work.

3.4.7 Model Performance

Using these phantoms, we could identify a set of model parameters with the potential to have particular utility due to invariance or sensitivity to orientation dispersion. Specifically, MD in DTI and intra-neurite volume fraction in both NODDI and Bingham-NODDI were largely

invariant to fibre crossing angle. This invariance means that they are potentially robust indicators of microstructural change in the presence of orientation dispersion. Meanwhile, ODI in NODDI and ODI_P in Bingham-NODDI both have strong relationships with fibre crossing angle, which suggests that they may be good indicators of orientation dispersion. The results also reveal potential overfitting of the volume fraction assigned to the extra-neurite and CSF compartments, which has also been observed in vivo [52]. However, some of this overfitting may also be attributed to the fixed CSF diffusivity being equal to the fixed axial diffusivity in these phantoms.

Some peculiarities with the phantom print quality led to a relatively low volume fraction of intra-pore space relative to the volume fraction of free water within the phantoms. While this structure was practically useful because it allowed water to reach and dissolve pockets of PVA in the elastomeric matrix more easily, it did seem to decrease the ability of both forms of NODDI to realistically describe the material. In both cases, volume fraction assigned to intra-neurite space was low relative to the volume fraction of extra-cellular space. This is not anatomically realistic, and caused NODDI to assign no volume fraction to CSF, and Bingham-NODDI to do the same in many voxels.

The design of the bending phantom in this study did not allow it to fully capture the effect of fibre curvature on model parameters. Several parameters followed a trend toward the distribution in the straight phantom as arc radius increased, but did not reach that distribution at the maximum arc radius included in the bending phantom (about 20 mm). Future work should include another bending phantom with arc radii above 20 mm to more fully explore the effect of fibre curvature on dMRI models.

3.5 Conclusions

The use of 3D printed phantoms as described in this work is a technique that allows dMRI model parameters from real data to be related to orientation dispersion without any significant

change in fibre microstructure. We have demonstrated the utility of the phantoms by using them to reveal existing models' relationships with fibre curvature and crossing angle. The phantoms can play a unique role in more in-depth treatments of existing models, and provide an inexpensive method for validating novel models using physically acquired data.

Chapter 4

Conclusions

We have introduced 3D printed axon-mimetic (3AM) phantoms, a novel class of diffusion MRI (dMRI) phantom that mimics axonal fibres well enough to draw conclusions about diffusion MRI models of white matter. 3AM phantoms fill a niche in the spectrum of dMRI phantoms that was empty. They are among the least expensive dMRI phantoms available to researchers, but are able to produce complex patterns of diffusion. Before 3AM phantoms, rigid capillaries or plain fibres were among the most accessible phantoms to researchers, and both are difficult to arrange in a more complex configuration than crossing fibres. 3AM phantoms can now become an easily accessible way to perform a phantom study of a dMRI model's response to orientation dispersion.

In the field of existing dMRI phantoms, 3AM phantoms are most similar to the membranes of hollow fibres produced by coaxial electrospinning [25]. Both phantom materials essentially produce fibrous pores that mimic intra-neurite restriction of diffusion, but make different trade-offs to produce that diffusion behaviour. By changing the parameters of the coaxial electrospinning process, the resulting hollow fibre diameter can be controlled. This is a particular advantage for assessing models that predict axon diameter, but is also useful for producing anatomically realistic fibre diameters. However, arranging the resulting membranes into complex fibre structures remains a challenge. The pore size characterization of 3AM phantoms

shown in Figure 2.3 shows that 3AM phantoms have reasonable pore sizes, but changing 3D print parameters does not have a significant effect on those pore sizes, so they are not customizable. FDM 3D printing is a necessary step for producing 3AM phantoms, which means that the fibre orientations can be customized in a straightforward way using inexpensive equipment. Thus, 3AM phantoms are a good choice when effects of orientation dispersion are of greater interest than effects of microstructural changes, or as an inexpensive first choice for exploratory phantom studies of dMRI models of white matter.

A limitation of the phantoms is that they have no physical analog to extra-neuronal hindering of diffusion. The micro-CT and microscopy images of 3AM phantoms shown in Chapter 2 demonstrates that each line of material has small fibrous pores embedded in the elastomeric matrix, rather than the tightly packed hollow fibres that make up axonal tracts in vivo. This limitation was made evident by NODDI's unstable fit to data from 3AM phantoms, as seen in Figure 3.6. 3AM phantoms have no analog to extra-neuronal space, so NODDI [12] struggles to consistently assign the balance between the isotropic and extra-neurite compartments. Still, 3AM phantoms compare favourably to other physical dMRI phantoms, and their unique flexibility enable phantom studies that would be difficult without them.

The study in Chapter 3 would have been difficult to perform with most existing phantoms, and very labour-intensive to perform with an ex-vivo tissue sample. Previously, this type of study that compares dMRI model fit to a signal to a ground truth of the fibre configuration that produced that signal would have been limited by practicality to a numerical phantom simulation. While the precise control of the ground truth offered by numerical phantoms is valuable, their validity as a prediction of a model's response to in-vivo data is limited by the validity of the model used to produce the simulation data. By offering a ground truth of fibre configuration associated with a physical object that can be scanned, 3AM phantoms offer scan data that includes the complexity inherent to a dMRI scan. The validity of the scan data is still limited by the difference between the 3AM phantom's fibrous pores and real axonal fibres, but 3AM phantoms can offer a useful complement to studies that would otherwise only have been

possible with simulations.

In Chapter 3, we demonstrated that utility of 3AM phantoms for characterizing a dMRI model's response to orientation dispersion. Every model we assessed was affected by fibre curvature, fibre crossings, or both, and no model was able to confine that effect to a single metric. Of the three signal representations under investigation (DTI, DKI, and ball and stick), only DTI's MD metric was robust to changes in crossing angle. This finding highlights that is important to be cognizant of orientational effects when trying to associate changes in dMRI model metrics with underlying microstructural changes. NODDI was largely successful at isolating the effect of orientation dispersion to its Orientation Dispersion Index, but it still saw a decrease in intra-neurite volume fraction with tighter fibre curvature. Fibre curvature is highly prevalent in the human brain, so this effect must be well understood and described before models like NODDI can see widespread clinical adoption. The findings presented in Chapter 3 are a useful reference in the development of that understanding, and the 3AM phantom study procedure could be applied to any number of other dMRI models.

Ultimately, the goal of dMRI research in neuroscience is to use dMRI to develop a better understanding of the brain's structure and how changes to that structure affect the function of the brain. Diffusion MRI signal representations and models of white matter are a critical bridge between raw dMRI signal and useful insight into the structure of the brain. So, by improving our understanding of the relation between dMRI model predictions and the underlying neural microstructure, we strengthen the validity of those predictions. In the broad landscape of tools for validating dMRI models, the need for a phantom that can flexibly represent a range of fibre configurations, is acceptably axon-mimetic, and is inexpensive for researchers to adopt is filled by the 3AM phantoms presented in this thesis.

4.1 Future work

The analysis performed with 3AM phantoms thus far has mostly been confined to investigating the effect of orientation dispersion within voxels in small, disc-shaped phantoms. However, there is significant interest in tractography techniques that map axonal tracts across different regions of the brain. To evaluate tractography methods, a large phantom composed of plain fibres compressed in a frame has been used to produce data with a ground truth [53]. A larger 3AM phantom with multiple interacting tracts existing on alternating layers could be produced with a similar effect, but would allow multiple sites to produce the same phantom without highly specialized equipment. The production of a large enough phantom for application of tractography would be a challenge, as regions deeper below the surface of the phantom would take longer for water to penetrate than any region in phantoms of the size considered in this thesis.

The 3AM phantoms used in this thesis had relatively low voxel-wise fibre densities, as indicated by intra-neurite volume fractions from 0.25 to 0.35 estimated by NODDI. One reason for this low fibre density is that even when the 3D printing software was instructed to depose lines of material directly adjacent to one another, small spaces remained between successive lines, as is visible in the top row of Figure 2.4. Resolving this issue and increasing the fibre density may result in higher and more anatomically realistic FA and associated metrics, alleviating some of the difference between 3AM phantom data and scan data of real tissue.

Bibliography

[1] D. B. Plewes and W. Kucharczyk, "Physics of MRI: A primer," *Journal of Magnetic Resonance Imaging*, vol. 35, pp. 1038–1054, May 2012.

[2] E. Vaghefi and P. J. Donaldson, "An Exploration into Diffusion Tensor Imaging in the Bovine Ocular Lens," *Frontiers in Physiology*, vol. 4, 2013.

[3] O. Sporns, G. Tononi, and R. Kötter, "The Human Connectome: A Structural Description of the Human Brain," *PLOS Computational Biology*, vol. 1, p. e42, Sept. 2005.

[4] D. C. Alexander, T. B. Dyrby, M. Nilsson, and H. Zhang, "Imaging brain microstructure with diffusion MRI: practicality and applications," *NMR in Biomedicine*, vol. 32, no. 4, p. e3841, 2019.

[5] S. Mori, *Introduction to Diffusion Tensor Imaging*. Introduction to Diffusion Tensor Imaging, Elsevier Science, 2007.

[6] D. S. Novikov, V. G. Kiselev, and S. N. Jespersen, "On modeling," *Magnetic Resonance in Medicine*, vol. 79, pp. 3172–3193, June 2018.

[7] R. L. Harms, F. J. Fritz, A. Tobisch, R. Goebel, and A. Roebroeck, "Robust and fast nonlinear optimization of diffusion MRI microstructure models," *NeuroImage*, vol. 155, pp. 82–96, July 2017.

[8] P. J. Basser, J. Mattiello, and D. LeBihan, "MR diffusion tensor spectroscopy and imaging," *Biophysical Journal*, vol. 66, pp. 259–267, Jan. 1994.

[9] J. H. Jensen, J. A. Helpern, A. Ramani, H. Lu, and K. Kaczynski, "Diffusional Kurtosis Imaging: The Quantification of Non-Gaussian Water Diffusion by Means of Magnetic Resonance Imaging," *Magnetic Resonance in Medicine*, vol. 53, no. 6, pp. 1432–1440, 2005.

[10] H. Lu, J. H. Jensen, A. Ramani, and J. A. Helpern, "Three-dimensional characterization of non-gaussian water diffusion in humans using diffusion kurtosis imaging," *NMR in Biomedicine*, vol. 19, no. 2, pp. 236–247, 2006.

[11] T. E. J. Behrens, M. W. Woolrich, M. Jenkinson, H. Johansen-Berg, R. G. Nunes, S. Clare, P. M. Matthews, J. M. Brady, and S. M. Smith, "Characterization and propagation of uncertainty in diffusion-weighted MR imaging," *Magnetic Resonance in Medicine*, vol. 50, no. 5, pp. 1077–1088, 2003.

[12] H. Zhang, T. Schneider, C. A. Wheeler-Kingshott, and D. C. Alexander, "NODDI: Practical in vivo neurite orientation dispersion and density imaging of the human brain," *NeuroImage*, vol. 61, pp. 1000–1016, July 2012.

[13] M. Tariq, T. Schneider, D. C. Alexander, C. A. Gandini Wheeler-Kingshott, and H. Zhang, "Bingham–NODDI: Mapping anisotropic orientation dispersion of neurites using diffusion MRI," *NeuroImage*, vol. 133, pp. 207–223, June 2016.

[14] I. O. Jelescu and M. D. Budde, "Design and Validation of Diffusion MRI Models of White Matter," *Frontiers in Physics*, vol. 5, 2017.

[15] T. B. Dyrby, G. M. Innocenti, M. Bech, and H. Lundell, "Validation strategies for the interpretation of microstructure imaging using diffusion MRI," *NeuroImage*, vol. 182, pp. 62–79, Nov. 2018.

[16] E. Fieremans and H.-H. Lee, "Physical and numerical phantoms for the validation of brain microstructural MRI: A cookbook," *NeuroImage*, vol. 182, pp. 39–61, Nov. 2018.

[17] D. Liewald, R. Miller, N. Logothetis, H.-J. Wagner, and A. Schüz, "Distribution of axon diameters in cortical white matter: an electron-microscopic study on three human brains and a macaque," *Biological Cybernetics*, vol. 108, pp. 541–557, Oct. 2014.

[18] J.-D. Tournier, S. Mori, and A. Leemans, "Diffusion tensor imaging and beyond," *Magnetic Resonance in Medicine*, vol. 65, no. 6, pp. 1532–1556, 2011.

[19] P. J. Basser, "Inferring microstructural features and the physiological state of tissues from diffusion-weighted images," *NMR in Biomedicine*, vol. 8, pp. 333–344, Nov. 1995.

[20] E. Fieremans, Y. D. Deene, S. Delputte, M. S. Özdemir, E. Achten, and I. Lemahieu, "The design of anisotropic diffusion phantoms for the validation of diffusion weighted magnetic resonance imaging," *Physics in Medicine & Biology*, vol. 53, p. 5405, Sept. 2008.

[21] C.-P. Lin, V. J. Wedeen, J.-H. Chen, C. Yao, and W.-Y. I. Tseng, "Validation of diffusion spectrum magnetic resonance imaging with manganese-enhanced rat optic tracts and ex vivo phantoms," *NeuroImage*, vol. 19, pp. 482–495, July 2003.

[22] D. Benjamini, M. E. Komlosh, P. J. Basser, and U. Nevo, "Nonparametric pore size distribution using d-PFG: Comparison to s-PFG and migration to MRI," *Journal of Magnetic Resonance*, vol. 246, pp. 36–45, Sept. 2014.

[23] M. E. Komlosh, E. Özarslan, M. J. Lizak, F. Horkay, V. Schram, N. Shemesh, Y. Cohen, and P. J. Basser, "Pore diameter mapping using double pulsed-field gradient MRI and its validation using a novel glass capillary array phantom," *Journal of Magnetic Resonance*, vol. 208, pp. 128–135, Jan. 2011.

[24] C. Guise, M. M. Fernandes, J. M. Nóbrega, S. Pathak, W. Schneider, and R. Fangueiro, "Hollow Polypropylene Yarns as a Biomimetic Brain Phantom for the Validation of High-Definition Fiber Tractography Imaging," *ACS Applied Materials & Interfaces*, vol. 8, pp. 29960–29967, Nov. 2016.

[25] F.-L. Zhou, P. L. Hubbard, S. J. Eichhorn, and G. J. Parker, "Coaxially Electrospun Axon-Mimicking Fibers for Diffusion Magnetic Resonance Imaging," *ACS Applied Materials & Interfaces*, vol. 4, pp. 6311–6316, Nov. 2012.

[26] F.-L. Zhou, P. L. Hubbard, S. J. Eichhorn, and G. J. M. Parker, "Jet deposition in near-field electrospinning of patterned polycaprolactone and sugar-polycaprolactone core–shell fibres," *Polymer*, vol. 52, pp. 3603–3610, July 2011.

[27] E. Fieremans, Y. De Deene, S. Delputte, M. S. Özdemir, Y. D'Asseler, J. Vlassenbroeck, K. Deblaere, E. Achten, and I. Lemahieu, "Simulation and experimental verification of the diffusion in an anisotropic fiber phantom," *Journal of Magnetic Resonance*, vol. 190, pp. 189–199, Feb. 2008.

[28] P. Pullens, A. Roebroeck, and R. Goebel, "Ground truth hardware phantoms for validation of diffusion-weighted MRI applications," *Journal of Magnetic Resonance Imaging*, vol. 32, no. 2, pp. 482–488, 2010.

[29] F. B. Laun, S. Huff, and B. Stieltjes, "On the effects of dephasing due to local gradients in diffusion tensor imaging experiments: relevance for diffusion tensor imaging fiber phantoms," *Magnetic Resonance Imaging*, vol. 27, pp. 541–548, May 2009.

[30] E. Farrher, J. Kaffanke, A. A. Celik, T. Stöcker, F. Grinberg, and N. J. Shah, "Novel multisection design of anisotropic diffusion phantoms," *Magnetic Resonance Imaging*, vol. 30, pp. 518–526, May 2012.

[31] S. O. Abu-Sardanah, U. Hussain, J. Moore, C. Baron, T. Peters, and A. R. Khan, "Design and evaluation of a diffusion MRI fibre phantom using 3D printing," in *Proc. SPIE 10573*, International Society for Optics and Photonics, Mar. 2018.

[32] A. J. Steven, J. Zhuo, and E. R. Melhem, "Diffusion Kurtosis Imaging: An Emerging Technique for Evaluating the Microstructural Environment of the Brain," *American Journal of Roentgenology*, vol. 202, pp. W26–W33, Dec. 2013.

[33] L. Beltrachini, Z. A. Taylor, and A. F. Frangi, "A parametric finite element solution of the generalised Bloch–Torrey equation for arbitrary domains," *Journal of Magnetic Resonance*, vol. 259, pp. 126–134, Oct. 2015.

[34] D. S. Grebenkov, "Exploring diffusion across permeable barriers at high gradients. II. Localization regime," *Journal of Magnetic Resonance*, vol. 248, pp. 164–176, Nov. 2014.

[35] A. Seehaus, A. Roebroeck, M. Bastiani, L. Fonseca, H. Bratzke, N. Lori, A. Vilanova, R. Goebel, and R. Galuske, "Histological validation of high-resolution DTI in human post mortem tissue," *Frontiers in Neuroanatomy*, vol. 9, 2015.

[36] T. B. Leergaard, N. S. White, A. d. Crespigny, I. Bolstad, H. D'Arceuil, J. G. Bjaalie, and A. M. Dale, "Quantitative Histological Validation of Diffusion MRI Fiber Orientation Distributions in the Rat Brain," *PLOS ONE*, vol. 5, p. e8595, Jan. 2010.

[37] A. Rokem, J. D. Yeatman, F. Pestilli, K. N. Kay, A. Mezer, S. v. d. Walt, and B. A. Wandell, "Evaluating the Accuracy of Diffusion MRI Models in White Matter," *PLOS ONE*, vol. 10, p. e0123272, Apr. 2015.

[38] Q. Fan, A. Nummenmaa, B. Wichtmann, T. Witzel, C. Mekkaoui, W. Schneider, L. L. Wald, and S. Y. Huang, "Validation of diffusion MRI estimates of compartment size and volume fraction in a biomimetic brain phantom using a human MRI scanner with 300 mT/m maximum gradient strength," *NeuroImage*, vol. 182, pp. 469–478, Nov. 2018.

[39] K. G. Schilling, Y. Gao, I. Stepniewska, V. Janve, B. A. Landman, and A. W. Anderson, "Histologically derived fiber response functions for diffusion MRI vary across white matter fibers—An ex vivo validation study in the squirrel monkey brain," *NMR in Biomedicine*, vol. 32, no. 6, p. e4090, 2019.

[40] N. Yanasak and J. Allison, "Use of capillaries in the construction of an MRI phantom for the assessment of diffusion tensor imaging: demonstration of performance," *Magnetic Resonance Imaging*, vol. 24, pp. 1349–1361, Dec. 2006.

[41] P. L. Hubbard, F.-L. Zhou, S. J. Eichhorn, and G. J. M. Parker, "Biomimetic phantom for the validation of diffusion magnetic resonance imaging," *Magnetic Resonance in Medicine*, vol. 73, pp. 299–305, Jan. 2015.

[42] F. M. Mushtaha, T. K. Kuehn, J. Moore, A. R. Khan, and C. A. Baron, "Microstructural characterization and validation of a 3D printed phantom for diffusion MRI," in *Proceedings of the 27th Annual Meeting of ISMRM*, (Montreal, Canada), 2019.

[43] D. Bradley and G. Roth, "Adaptive Thresholding using the Integral Image," *Journal of Graphics Tools*, vol. 12, pp. 13–21, Jan. 2007.

[44] E. Garyfallidis, M. Brett, B. Amirbekian, A. Rokem, S. Van Der Walt, M. Descoteaux, and I. Nimmo-Smith, "Dipy, a library for the analysis of diffusion MRI data," *Frontiers in Neuroinformatics*, vol. 8, 2014.

[45] R. Mills, "Self-diffusion in normal and heavy water in the range 1-45.deg.," *The Journal of Physical Chemistry*, vol. 77, pp. 685–688, Mar. 1973.

[46] A. L. Alexander, J. E. Lee, M. Lazar, and A. S. Field, "Diffusion tensor imaging of the brain," *Neurotherapeutics*, vol. 4, pp. 316–329, July 2007.

[47] J. H. Jensen, M. F. Falangola, C. Hu, A. Tabesh, O. Rapalino, C. Lo, and J. A. Helpern, "Preliminary observations of increased diffusional kurtosis in human brain following recent cerebral infarction," *NMR in biomedicine*, vol. 24, pp. 452–457, June 2011.

[48] A. L. Alexander, K. M. Hasan, M. Lazar, J. S. Tsuruda, and D. L. Parker, "Analysis of partial volume effects in diffusion-tensor MRI," *Magnetic Resonance in Medicine*, vol. 45, no. 5, pp. 770–780, 2001.

[49] B. Jeurissen, A. Leemans, J.-D. Tournier, D. K. Jones, and J. Sijbers, "Investigating the prevalence of complex fiber configurations in white matter tissue with diffusion magnetic resonance imaging," *Human Brain Mapping*, vol. 34, no. 11, pp. 2747–2766, 2013.

[50] F. N. Mushtaha, T. K. Kuehn, O. El-Deeb, S. A. Rohani, L. W. Helpard, J. Moore, H. Ladak, A. Moehring, C. A. Baron, and A. R. Khan, "Microstructural characterization and validation of a 3D printed phantom for diffusion MRI," *bioRxiv*, p. 2020.07.02.185397, July 2020.

[51] S. Lasič, F. Szczepankiewicz, S. Eriksson, M. Nilsson, and D. Topgaard, "Microanisotropy imaging: quantification of microscopic diffusion anisotropy and orientational order parameter by diffusion MRI with magic-angle spinning of the q-vector," *Frontiers in Physics*, vol. 2, 2014.

[52] P. McCunn, K. M. Gilbert, P. Zeman, A. X. Li, M. J. Strong, A. R. Khan, and R. Bartha, "Reproducibility of Neurite Orientation Dispersion and Density Imaging (NODDI) in rats at 9.4 Tesla," *PLOS ONE*, vol. 14, p. e0215974, Apr. 2019.

[53] P. Fillard, M. Descoteaux, A. Goh, S. Gouttard, B. Jeurissen, J. Malcolm, A. Ramirez-Manzanares, M. Reisert, K. Sakaie, F. Tensaouti, T. Yo, J.-F. Mangin, and C. Poupon, "Quantitative evaluation of 10 tractography algorithms on a realistic diffusion MR phantom," *NeuroImage*, vol. 56, pp. 220–234, May 2011.

Appendix A

3AM Phantom Production Protocol

Materials and equipment

- GEL-LAY filament
- Surfactant
- Test tubes
- Airtight test tube stoppers
- Clear plastic container
- Deionized water
- Phantom cylinder STL file (example available at osf.io/dz8rf/)
- FDM 3D printer (must be compatible with Cura)
- Vacuum chamber
- Cage with individual chambers for each phantom

Safety

After 3D printing, handle phantoms with gloves at all times.

Storage

- GEL-LAY filament
  - The quality of the filament can be affected by moisture in the air. Store the spool of GEL-LAY according to manufacturer's recommendations, or in a sealed bag with packets of silica gel.
- 3AM phantoms
  - The phantoms can be immersed in tap water during the dissolving phase, but must be immersed in distilled water in their final preparation for dMRI scanning.

Preparing phantoms for dMRI scanning

1. For each phantom, use Cura to load the STL file, ensure the nominal print parameters are selected according to Table A.1, and choose your desired infill pattern.
2. Arrange the phantoms in the cage, recording the position of each phantom.
3. Place the cage filled with phantoms in a clear plastic container filled with room temperature tap water. It may be necessary to place a weight on the cage to prevent it from floating to the surface.
4. Let the phantoms dissolve for 7 to 10 days, emptying the container and refilling it with water every day to avoid saturation and PVA build up.
5. Empty the container of tap water and refill it with deionized water.

6. Add 1/20th part surfactant to the deionized water.

7. Place the plastic container in the vacuum chamber, and run the vacuum pump until the chamber reaches 1 bar pressure.

8. Leave the container in the vacuum chamber for 48 hours.

9. Prepare the test tubes by labelling them and rinsing them with deionized water.

10. Keeping everything underwater, move the phantoms from the cage into the test tubes, noting the order in which the phantoms are placed.

11. Seal the test tube with a stopper and remove it from the container.

Note: It is crucial that after the phantoms are removed from the vaccum chamber, they are kept underwater and make no contact with air.

Printing parameter	Nominal value
Printing temperature (°C)	225
Printing speed (mm/s)	30
Layer thickness (mm)	0.1
Infill density (%)	100

Table A.1: Nominal phantom printing parameters

Appendix B

Copyright Permission

See the following images for documentation of the permission referred to in the caption of Figure 1.1.

JOHN WILEY AND SONS LICENSE
TERMS AND CONDITIONS

Jul 29, 2020

This Agreement between Mr. Tristan Kuehn ("You") and John Wiley and Sons ("John Wiley and Sons") consists of your license details and the terms and conditions provided by John Wiley and Sons and Copyright Clearance Center.

License Number	4877680650900
License date	Jul 28, 2020
Licensed Content Publisher	John Wiley and Sons
Licensed Content Publication	Journal of Magnetic Resonance Imaging
Licensed Content Title	Physics of MRI: A primer
Licensed Content Author	Walter Kucharczyk, Donald B. Plewes
Licensed Content Date	Apr 12, 2012
Licensed Content Volume	35
Licensed Content Issue	5
Licensed Content Pages	17

Type of use	Dissertation/Thesis
Requestor type	University/Academic
Format	Print and electronic
Portion	Figure/table
Number of figures/tables	1
Will you be translating?	No
Title	A 3D-Printed Axon Mimetic Diffusion MRI Phantom
Institution name	University of Western Ontario
Expected presentation date	Aug 2020
Portions	Figure 1
Requestor Location	Mr. Tristan Kuehn 
Publisher Tax ID	EU826007151
Total	0.00 CAD

Curriculum Vitae

Tristan Kuehn

Education

Master of Engineering Science, Biomedical Engineering

Western University, September 2018 - August 2020 (Anticipated)

Bachelor of Applied Science, Systems Design Engineering

University of Waterloo, September 2013 - April 2018

Research Experience

Undergraduate Research Assistant

Waterloo Composite Biomaterial Systems Lab, University of Waterloo, Waterloo, ON, May 2017 - August 2017

Teaching Experience

Graduate Teaching Assistant for Foundations of Engineering Practice

Faculty of Engineering, Western University, London, ON, September 2019 - December 2019

Graduate Teaching Assistant for Circuits and Systems

Department of Electrical and Computer Engineering, Western University, London, ON, January 2019 - April 2019

Graduate Teaching Assistant for Digital Logic Systems

Department of Electrical and Computer Engineering, Western University, London, ON, September 2018 - December 2018

Publications

Kasa LW, Haast RAM, **Kuehn TK**, Mushtaha FN, Baron CA, Peters T, Khan AR. Evaluating High Spatial Resolution Diffusion Kurtosis Imaging at 3T: Reproducibility and Quality of Fit. Journal of Magnetic Resonance Imaging (Under Review).

Lau JC, Parrent AG, Demarco J, Gupta G, Kai J, Stanley OW, **Kuehn T**, Park PJ, Ferko K, Khan AR, Peters TM. A framework for evaluating correspondence between brain images using anatomical fiducials. Human Brain Mapping. 2019;40(14):4163-4179. doi:10.1002/hbm.24693.

Presentations

Kuehn TK, Mushtaha FN, El-Deeb O, Moehring A, Baron CA, Khan AR. (2020). Characterization of orientation dispersion's impact on diffusion kurtosis and NODDI using an axon-mimetic 3D printed phantom. Paper presented at the International Society for Magentic Resonance in Medicine Virtual Conference & Exhibition, August 8.

Mushtaha FN, **Kuehn TK**, El-Deeb O, Moehring A, Baron CA, Khan AR. (2020). An open framework for producing and analyzing diffusion MRI phantoms. Paper presented at the 2020 Organization for Human Brain Mapping Annual Meeting, July 24.

Mushtaha FN, **Kuehn TK**, Moore J, Khan AR, Baron CA. (2019). Microstructural characterization and validation of a 3D printed phantom for diffusion MRI. Paper presented at the International Society for Magentic Resonance in Medicine 27th Annual Meeting & Exhibition, Montreal, Canada, May 11.

Kuehn TK, Mushtaha FN, Moore J, Baron CA, Khan AR. (2019). Evaluation of Diffusion MRI Fibre Reconstruction with a 3D Printed Phantom. Paper presented at the 17th Annual Imaging Network Ontario Symposium, London, Canada, March 28.

Mushtaha FN, **Kuehn TK**, Moore J, Khan AR, Baron CA. (2019). Varying Microstructural Properties of a 3D Printed Phantom for Diffusion MRI Validation. Paper presented at the 17th Annual Imaging Network Ontario Symposium, London, Canada, March 28.

Awards

Graduation Dean's Honours List

University of Waterloo, May 2018

Graduation with Distinction

University of Waterloo, May 2018

First in Class Engineering Scholarship ($ 500)

University of Waterloo, January 2018

Undergraduate Student Research Award ($ 4500)

National Sciences and Engineering Research Council of Canada, May 2017

President's Research Award ($ 1500)

University of Waterloo, May 2017

President's Scholarship of Distinction ($ 2000)

University of Waterloo, September 2013